

Searching for photon-ALPs mixing effects in AGN gamma-ray energy spectra

Qixin Yu and Dieter Horns

Institut für Experimentalphysik, University of Hamburg, Luruper Chaussee 149, D-22761 Hamburg, Germany

E-mail: qixin.yu@desy.de, dieter.horns@physik.uni-hamburg.de

Abstract. High energy gamma-rays propagating in external magnetic fields may convert into axion-like particles (ALPs). In this case, the observed gamma-ray spectra are modified by the resulting energy-dependent conversion probability. In this study, we use the energy spectra of 20 extra-galactic gamma-ray sources recorded during 10 years of *Fermi*-LAT observations. We define a test statistics based upon the likelihood ratio to test the hypothesis for a spectral model without vs. a model with photon-ALPs coupling. The conversion probability is calculated for fixed values of the mass and two-photon coupling of the pseudo-scalar particle while the external magnetic field is characterized by the additional free parameters length scale s and average field strength B . As a consistency check and in order to extend the analysis to include very high energy gamma-ray data, another test statistics is defined with the χ^2 method. We find for 18 of the 20 sources a favorable fit, particularly for Markarian 421 and NGC 1275 a significant improvement, with the hypothesis of photon-ALPs coupling in likelihood analysis. The test statistics of the sources are combined and the significance has been estimated 5.3σ (test statistics summed in local maxima of all sources) and 6.0σ (global maxima). The significance is estimated from dedicated simulations under the null hypotheses. The locally best-fitting values of B and s fall into the range that is expected for large scale magnetic fields present in relevant astrophysical environments.

Keywords: photon-ALPs mixing — Blazars — *Fermi*-LAT

Contents

1	Introduction	1
2	Photon-ALP oscillation model and astrophysical magnetic fields	2
3	Source selection and data reduction	4
3.1	Source selection	4
3.2	<i>Fermi</i> -LAT data reduction	5
4	Analysis and Results	6
4.1	Spectral models	6
4.2	Parameter estimates: Null hypothesis	7
4.3	Parameter estimates: ALPs hypothesis	8
4.4	Hypotheses testing for the joined <i>Fermi</i> -LAT spectra	10
4.5	Combined HE and VHE spectra	13
4.5.1	Combined spectrum of PKS 2155-304	14
4.5.2	Combined spectrum from Mkn 421	15
5	Discussion	16
6	Summary	20
A	Additional fit-results	20

1 Introduction

Axions are pseudoscalars which are originally proposed as a solution to address the strong CP problem in quantum chromodynamics (QCD) [1, 2]. Besides the QCD axion, the existence of various axion-like particles (ALPs) has been predicted in the framework of extra-dimensional completions of the standard model [3–5]. ALPs are very light pseudo-scalar bosons (a) characterized mainly by a two-photon coupling $g_{a\gamma\gamma}$ and its mass m_a . Both, the QCD axion as well as ALPs are possible candidates for particle dark matter [6–9].

A non-vanishing coupling of ALPs to photons leads to a rich phenomenology for photon/ALPs mixing that can be observed in the universe and probed with laboratory experiments. While searches for axion/ALP type dark matter have so far only produced exclusion limits, astrophysical searches have been considered a promising approach to find signatures for photon-ALPs mixing in gamma-ray spectra [see e.g., 10–12]. There have been several claims for indications for anomalous TeV transparency [see e.g., 13–16] as well as modulation of spectra of Galactic sources [17]. In both cases, an interpretation of the observations has been put forward that singles out the mass range of neV and coupling constants $10^{-12} \text{ GeV}^{-1} < g_{a\gamma\gamma} < 10^{-10} \text{ GeV}^{-1}$ [17–19] where the uncertainties are mainly related to the assumption of the magnetic field present along the line of sight. The minimum value of the coupling would be accessible with the upcoming light-shining-through a wall experiment ALPS II [20].

The upper range of preferred coupling is in tension with the upper bounds of $g_{a\gamma\gamma} < 6.6 \times 10^{-11} \text{ GeV}^{-1}$ (95 % c.l.) from the CAST experiment that searches for ALPs generated

in the core of the sun and then re-converts to X-ray photons in the transversal magnetic field of the CAST magnet [21]. However, the conversion inside the sun may be modified, effectively suppressing the ALPs flux emitted by the sun [22].

Here, we extend the search for spectral modulations in high energy and very high energy gamma-ray data of a sample of high frequency peaked BL Lac type objects (HBL) and the radio galaxy NGC 1275. Different from previous studies where a particular model for the magnetic field is used and the values of the axion-related parameters are left free, we instead assume a fixed mass $m_a = 3.6 \text{ neV}$ and coupling $g_{a\gamma\gamma} = 2.3 \times 10^{-10} \text{ GeV}^{-1}$ motivated by [17] and leave the constant magnetic field strength and its spatial extension as free parameters.

In the following sections, we present the calculation for the conversion probability in astrophysical magnetic fields (Sec. 2), the source selection and reconstruction of energy spectra (Sec. 3), and the results in Sec. 4.

2 Photon-ALP oscillation model and astrophysical magnetic fields

The photon-ALP oscillation effect occurs in the presence of an external magnetic field. The photon-ALP coupling is described by the following Lagrangian [23]:

$$\mathcal{L} = -\frac{1}{4}g_{a\gamma\gamma}aF_{\mu\nu}\tilde{F}^{\mu\nu} = g_{a\gamma\gamma}a\mathbf{E} \cdot \mathbf{B}, \quad (2.1)$$

where $g_{a\gamma\gamma}$ is the coupling constant between ALPs and photons, a is the ALP field, $F_{\mu\nu}$ is the electromagnetic field tensor, $\tilde{F}^{\mu\nu}$ is its dual tensor. \mathbf{E} and \mathbf{B} are the electric and magnetic fields, respectively. Considering an initially polarized photon beam propagating through a single homogeneous magnetic field domain, the propagation equation can be written in a Schrödinger-like form:

$$\left(i\frac{d}{dx_3} + E + \mathcal{M}\right)\Psi(x_3) = 0, \quad (2.2)$$

with

$$\Psi(x_3) = (A_1(x_3), A_2(x_3), a(x_3))^T, \quad (2.3)$$

where $A_1(x_3)$ and $A_2(x_3)$ are the photon linear polarization states along x_1 and x_2 axis respectively, $a(x_3)$ denotes the ALP state. \mathcal{M} represents the photon-ALP mixing matrix.

The mixing matrix could be simplified in the case where \mathbf{B} is homogeneous. Here we use \mathbf{B}_T the transverse magnetic field, and B_1 vanishes if \mathbf{B}_T is chosen to be along the x_2 axis. We denote the photon polarization state parallel to the transverse magnetic field \mathbf{B}_T direction by A_{\parallel} , and the orthogonal one by A_{\perp} . In this way \mathcal{M} can be simplified and written as [14, 24, 25]

$$\mathcal{M} = \begin{pmatrix} \Delta_{\perp} & 0 & 0 \\ 0 & \Delta_{\parallel} & \Delta_{a\gamma} \\ 0 & \Delta_{a\gamma} & \Delta_a \end{pmatrix}, \quad (2.4)$$

where the terms $\Delta_{\perp} \equiv \Delta_{\text{pl}} + \Delta_{\parallel}^{\text{CM}} + \Delta_{\text{CMB}}$, $\Delta_{\parallel} \equiv \Delta_{\text{pl}} + \Delta_{\parallel}^{\text{CM}} + \Delta_{\text{CMB}}$, $\Delta_{a\gamma} \equiv \frac{1}{2}g_{a\gamma\gamma}B_T$ and $\Delta_a \equiv -\frac{m_a^2}{2E}$ [14, 23], where m_a is the mass of the ALP, Δ_{pl} stands for plasma effects and has the form

$$\Delta_{\text{pl}} \equiv -\frac{\omega_{\text{pl}}^2}{2E} \simeq -1.1 \times 10^{-10} \times \left(\frac{E}{\text{TeV}}\right)^{-1} \times \left(\frac{n_e}{10^{-3} \text{ cm}^{-3}}\right) \text{ kpc}^{-1}, \quad (2.5)$$

where $\omega_{\text{pl}} = \sqrt{4\pi n_e e^2 / m_e}$ is the plasma frequency and n_e is the electron density in the medium (typical value of n_e used here is $1.1 \times 10^{-2} \text{ cm}^{-3}$ [26]). The terms $\Delta_{\parallel, \perp}^{\text{CM}}$ (Cotton-Mouton effect) are associated with the birefringence effects of the vacuum expected from the Euler-Heisenberg Lagrangian in the presence of transverse magnetic field, and the term Δ_{CMB} accounts for photon-photon dispersion [27]. In the following, we neglect the effects of birefringence and photon-photon dispersion since they do not affect the energy range covered with *Fermi*-LAT. We list the relevant parameters for numerical calculation [14]:

$$\Delta_{a\gamma} \simeq 7.6 \times 10^{-2} \times \left(\frac{g_{a\gamma\gamma}}{5 \times 10^{-11} \text{ GeV}^{-1}} \right) \times \left(\frac{B_T}{\mu G} \right) \text{ kpc}^{-1}, \quad (2.6)$$

$$\Delta_a \simeq -7.8 \times 10^{-3} \left(\frac{m_a}{10 \text{ neV}} \right)^2 \times \left(\frac{E}{\text{TeV}} \right)^{-1} \text{ kpc}^{-1}. \quad (2.7)$$

For the simplest case of a large-scale homogeneous magnetic field, the probability of a photon oscillating into an ALP (or vice versa) after traveling a distance s is

$$p_{\gamma \rightarrow a} = \frac{4\Delta_{a\gamma}^2}{\Delta_{\text{osc}}^2} \sin^2 \left(\frac{s \Delta_{\text{osc}}}{2} \right), \quad (2.8)$$

where the oscillation wave number Δ_{osc} has the form

$$\Delta_{\text{osc}} \equiv \sqrt{(\Delta_a - \Delta_{\text{pl}})^2 + 4\Delta_{a\gamma}^2}. \quad (2.9)$$

Furthermore, it can be seen from Eq. (2.8) that the photon-ALP mixing becomes maximal and energy-independent when $E \gg E_c$ given by

$$E_c \equiv \frac{E |\Delta_a - \Delta_{\text{pl}}|}{2\Delta_{a\gamma}}. \quad (2.10)$$

This is similar to the resonant case, where $\Delta_a = \Delta_{\text{pl}}$.

In order to take into account photon absorption, e.g., by interaction with a soft photon background field, the photon-ALP system is then described by a modified Schrödinger-like equation similar to Eq. (2.2), and can be written as [13, 23, 27, 28]

$$\left(i \frac{d}{dx_3} + E + \mathcal{M} + iD \right) \Psi(x_3) = 0, \quad (2.11)$$

with the additional matrix

$$D = \begin{pmatrix} \mathcal{C}(x_3) & 0 & 0 \\ 0 & \mathcal{C}(x_3) & 0 \\ 0 & 0 & 0 \end{pmatrix},$$

with $\mathcal{C}(x_3)$ related to the optical depth $\tau(x_3)/2 = \int_0^{x_3} \mathcal{C}(x'_3) dx'_3$.

The formal solution of Eq. 2.11 is then given for an initial condition $\Psi(0)$:

$$\Psi(x_3) = \exp \left(-i \int_0^{x_3} (E + \mathcal{M} - iD) dx'_3 \right) \Psi(0). \quad (2.12)$$

Then, the surviving probability of the photon in photon-ALP system can be given by [13, 14]:

$$p_{\gamma\gamma} = |A_1(x_3)|^2 + |A_2(x_3)|^2. \quad (2.13)$$

This formalism can be readily extended to consider un-polarized initial states by introducing the density matrix formalism and a von-Neumann type equation instead of the Schrödinger-type equation (2.11) [23, 28]. As for the magnetic fields along the propagation of photon-ALP beam, we consider three distinct regions for conversion: the source and its vicinity, the intergalactic space, and the Milky Way. The magnetic field strength and structure present in the Milky Way is fairly well known via observations of Faraday-rotation measures, the polarization of the emission from aligned dust grains and more indirectly through the synchrotron emissivity of the interstellar medium. The magnetic field of intergalactic space is only constrained to be smaller than $\approx \text{nG}$ [29] and not to be lower than $\approx 10^{-16} \text{ G}$ [30]. Finally, the magnetic field of the sources and their neighborhood is poorly known and may differ from source to source.

The photon-ALP mixing effect in the intergalactic magnetic field (IGMF) is neglected here, similar to previous studies [14]. In this case, the propagation can be separated into three regions. In the source region, we obtain the solution using Eq. (2.12), neglecting absorption $\mathcal{C} = 0$. In the IGMF, we do not consider the mixing, such that for the solution in Eq. (2.12), we assume $\mathcal{M} \approx 0$. Finally, in the Milky Way, we neglect additional absorption ($\mathcal{C} \approx 0$) caused by local radiation fields.

The magnetic field of the source and its environment is characterized by a minimal set of parameters used here: the strength of the transversal magnetic field B and its characteristic coherence length s . The conversion in the Milky Way is calculated using the model of the galactic magnetic field (GMF) from Ref. [31] taking into account the line of sight of individual sources.

3 Source selection and data reduction

3.1 Source selection

The sensitivity for signatures of photon-ALPs conversion in high energy gamma-ray spectra is related to the uncertainties on the differential flux measurements. Conversely, the appearance of modulations in the gamma-ray spectra requires a sufficiently large conversion probability $p_{\gamma \rightarrow a}$ (see Eq. (2.8)). Large distances with a sizeably transverse magnetic field are favorable conditions to search for such modulations. While in the previous study by [17], Galactic pulsars were used, we extend the search to extra-galactic objects.

Almost all extra-galactic gamma-ray sources are associated with active galactic nuclei (AGN). In order to cover a large range of energies with AGN spectra, we select objects which have a hard gamma-ray spectrum and are sufficiently bright to measure the differential flux accurately. In order to collect our source sample, the following selection cuts are applied to the fourth *Fermi*-LAT source catalogue, 4FGL [32]:

1. Source type (association): AGN of BL Lac type.
2. Red shift: z known or constrained $z < 0.5$.
3. TeV association: in order to potentially extend to very high energies (VHE: $E > 100 \text{ GeV}$), we require the sources to have an association to known VHE sources (*TeVCAT* flag).
4. Hard spectrum: photon index is smaller than 2.
5. Signal-to-noise ratio: detection significance larger than 50 standard deviations.

6. Photon statistics: number of predicted photons (N_{pred}) should exceed 1600.

Table 1. AGN sources selected for this study (in order of right ascension). The information listed are Galactic longitude (l) and latitude (b), red shift (z). Also, detection significance, photon index, and predicted event counts from Fermi 4FGL catalog.

AGN name	Source type	$l[^{\circ}]$	$b[^{\circ}]$	z	Detection signif. (σ)	Photon index	N_{pred}
1ES 0033+595	HBL	120.90	-3.02	0.467	68	1.765	2954
3C 66A	IBL	140.15	-16.76	0.34	182	1.971	15207
PKS 0301-243	HBL	214.63	-60.19	0.2657	108	1.914	5623
NGC 1275	Radio Galaxy	150.58	-13.26	0.017559	245	2.114	35561
PKS 0447-439	HBL	248.81	-39.91	0.343	167	1.865	12536
1ES 0502+675	HBL	143.79	15.89	0.34	64	1.601	1718
1ES 0806+524	HBL	166.25	32.94	0.138	100	1.881	5147
1ES 1011+496	HBL	165.53	52.71	0.212	169	1.838	9806
Markarian 421	HBL	179.88	65.01	0.031	344	1.781	30562
Markarian 180	HBL	131.91	45.64	0.045	50	1.798	1623
1ES 1215+303	HBL	189.01	82.05	0.131	146	1.933	10779
1ES 1218+304	HBL	182.21	82.74	0.182	83	1.722	3285
PKS 1440-389	HBL	325.65	18.71	0.1385	78	1.845	3788
PG 1553+113	HBL	21.92	43.96	$\lesssim 0.5$	120	1.681	10046
Markarian 501	HBL	63.60	38.86	0.034	173	1.790	11127
1ES 1727+502	HBL	77.07	33.54	0.055	60	1.790	2251
1ES 1959+650	HBL	98.00	17.67	0.048	169	1.817	11700
PKS 2005-489	HBL	350.37	-32.61	0.071	70	1.838	3115
PKS 2155-304	HBL	17.74	-52.25	0.116	239	1.850	17766
1ES 2344+514	HBL	112.89	-9.90	0.044	71	1.811	3201

The 19 sources passing the selection cuts are listed in Table 1. Additionally, we include one more source, a well-known and bright radio galaxy, NGC 1275. This source is located at the center of the Perseus galaxy cluster which most likely supports an extended [33] as well as a turbulent magnetic field [34]. This magnetized environment is favourable for photon-ALPs mixing and has already motivated several authors to search for spectral irregularities in the *Fermi*-LAT energy spectrum of NGC 1275 [16, 22, 35].

3.2 *Fermi*-LAT data reduction

In this study, we make use of 10 years of LAT data taken in the period from Aug. 4, 2008 to Aug. 4, 2018 in the energy range from 100 MeV to 500 GeV. We select events within a region of interest (ROI) defined as a cone centered on each source with a half-opening angle of 10° .

The events are selected by applying a zenith cut of 90° to minimize the γ -ray contributions from the Earth's limb. We set the spatial bin size to be 0.1° and distribute 48 energy bins (corresponds to 13 bins per decade) within the selected energy range

for performing a binned likelihood analysis. Following the recommendations of the LAT instrument team, the energy dispersion is corrected by introducing 3 additional bins beyond the energy range analysed.

The LAT data processed in pass 8 (release 3, version 2) have been downloaded together with the spacecraft file and the matching instrumental response files (`P8R3_SOURCE_V2` IRFs) from the Fermi Science Data Center. Subsequently, the events of class *source* with conversion in front and back part of the tracker are selected. The preparatory steps of the data analysis include creation of live time cube, data cubes etc. These tasks have been carried out using the `Fermi Science Tools ver1.2.23`¹ [36]. Most of these steps of the data reduction have been conveniently performed with the python based `fermipy ver0.19.0`² interface.

The diffuse backgrounds are modeled with pre-processed templates of the Galactic diffuse emission, `gll_iem_v07.fits`, and the extra-galactic isotropic radiation, `iso_P8R3_SOURCE_V2_v1.txt`. The energy dispersion for the background templates is already taken into account³. Point sources from the *Fermi*-LAT fourth catalog (4FGL, [37]), within a region of 15° , are included to the source model.

The resulting energy spectra are displayed as spectral energy distributions (SEDs). The SEDs are derived by taking the differential flux measurements and multiplying the individual flux values in each bin by the squared geometrical mean energy of the bin.

4 Analysis and Results

4.1 Spectral models

The energy spectra of the sources listed in Table 1 are compared with two different models that follow from the two hypotheses considered here. The hypothesis $H_0(\overline{ALPS})$ “without” photon-ALPs mixing is the null hypothesis and the alternative is $H_1(ALPS)$ “with” photon-ALPs mixing.

In our spectral analysis, the intrinsic model of any AGN is either described by the *Logparabola* model or in a few cases by a single *PowerLaw*, as given in Eqs. (4.1) and (4.2) respectively.

$$\left(\frac{dN}{dE}\right)_{intr.} = N_0 \left(\frac{E}{E_b}\right)^{-(\alpha + \beta \ln(E/E_b))}, \quad (4.1)$$

where the free parameters N_0 is the normalization factor at scale energy E_b , which is usually held constant, α is the power-law index and β the curvature parameter.

$$\left(\frac{dN}{dE}\right)_{intr.} = N_0 \left(\frac{E}{E_b}\right)^{-\alpha}, \quad (4.2)$$

The choice of the spectral model is based upon the LAT 8-year source catalog (4FGL) [37].

The intrinsic spectrum is subsequently modified by absorption via pair-production on the soft extra-galactic background light (EBL). The optical depth $\tau_{\gamma\gamma}(E)$ relies on the choice of an EBL model. Since the optical depth in the energy and red shift range considered here is small ($\tau_{\gamma\gamma} \ll 1$), the actual choice of the model is not of importance for the results obtained

¹<https://fermi.gsfc.nasa.gov/ssc/data/analysis/documentation/>

²<https://fermipy.readthedocs.io/en/latest/>

³<https://fermi.gsfc.nasa.gov/ssc/data/analysis/documentation/>

here, but needs to be included. The model of [38] is used as it is conveniently integrated in the PhotonALPsConv package⁴.

Under the alternative hypothesis H_1 with photon-ALP mixing, the spectrum is multiplied with the photon surviving probability $p_{\gamma\gamma}$. It is a function of photon energy E , ALP mass m_a , photon-ALP coupling $g_{a\gamma\gamma}$, transversal (constant) B-field strength B and the distance s over which the B-field is present.

In order to make the general problem of estimating the free parameters numerically tractable, we consider m_a and $g_{a\gamma\gamma}$ fixed at values which have been found to be favorable to explain spectral modulations present in energy spectra of Galactic pulsars [17]. The resulting best estimates have been found to be $m_a = 3.6 \text{ neV}$, $g_{a\gamma\gamma} = 2.3 \times 10^{-10} \text{ GeV}^{-1}$.

Therefore, the spectra modeled in this way for the two hypotheses (with and without photon-ALP conversion) would have the following forms:

$$H_0 : \quad \left(\frac{dN}{dE} \right)_{w/o \text{ ALP}} = e^{-\tau_{\gamma\gamma}} \left(\frac{dN}{dE} \right)_{intr.}, \quad (4.3)$$

and

$$H_1 : \quad \left(\frac{dN}{dE} \right)_{w/ \text{ ALP}} = \left(\frac{dN}{dE} \right)_{intr.} p_{\gamma\gamma}(E, m_a, g_{a\gamma\gamma}, B, s), \quad (4.4)$$

respectively, where $(dN/dE)_{intr.}$ is the source model referring to Eq. (4.1) or Eq. (4.2), and photon survival probability $p_{\gamma\gamma}$ in Eq. (4.4) is calculated with Eq. (2.13).

4.2 Parameter estimates: Null hypothesis

We fit the experimental data with two different approaches using as test statistics separately the log likelihood ratio and $\Delta\chi^2$. For the likelihood fitting of the SED we use the forward-folding method as implemented in the *fermitools*. This way, we determine the likelihood value for the best-fitting model for both hypotheses H_0 and H_1 . The effect of the survival probability $p_{\gamma\gamma}$ is implemented by calling the *gtlike* tool with a so-called *filefunction* model. For each value of B and s chosen, we optimize the parameters of $(dN/dE)_{intr.}$ using the likelihood fitting method.

In order to check for consistency and to be more flexible to include additional data sets (e.g. VHE spectra), we also implement a χ^2 fitting method with the definition for the *Fermi*-LAT data

$$\chi^2 = \sum_{i=1}^N \frac{(D_{ij}\Psi_j - \phi_i)^2}{\sigma_i^2}, \quad (4.5)$$

where N is the number of energy bins ($N = 18$ for all sources analyzed with χ^2 method), $D_{ij}\Psi_j$ and ϕ_i are respectively the expected and observed γ -ray flux in bin i with a statistical uncertainty σ_i . The model flux Ψ_j is corrected using the energy dispersion matrix D_{ij} determined for the particular observation using the tool *gtdrm* with one additional bin added to the lower and upper end of the spectrum⁵.

In Table 2, we list the best-fitting parameters estimated under the null hypothesis with the likelihood method (for χ^2 estimates, see Table 5 in Appendix A). For each source, we find a maximum likelihood L_{max}^0 (resp. a minimum $\chi_{w/o\text{ALP}}^2$) with the best-fitting normalization value N_0 , the power-law index α , the curvature parameter β and the scaling energy E_b . The uncertainties listed are calculated for a 68 % confidence interval.

⁴<https://github.com/me-manu/PhotALPsConv>

⁵https://fermi.gsfc.nasa.gov/ssc/data/analysis/documentation/Pass8_edisp_usage.html

Table 2. Best-fitting parameters for null hypothesis with likelihood method using the modeled spectra from Eq. (4.3), where sources with no curvature parameter are modeled with *PowerLaw*, and the rest is with *Logparabola*. The normalization is given in units of $10^{-12}\text{MeV}^{-1}\text{cm}^{-2}\text{s}^{-1}$. The estimated uncertainties (1σ) are listed as well (except for the scaling energy E_b which is kept fixed at the value from the catalogue).

AGN name	N_0	α	β $\times 10^{-3}$	E_b [MeV]
1ES 0033+595	0.363(0.015)	1.68(0.03)	-4(12)	3177
3C 66A	10.9(0.1)	1.88(0.01)	39(4)	1211
PKS 0301-243	5.66(0.12)	1.83(0.02)	31(8)	954.4
NGC 1275	56.1(0.4)	2.04(0.004)	60(3)	883.6
PKS 0447-439	4.62(0.07)	1.74(0.01)	52(5)	1605
1ES 0502+675	0.0593(0.0026)	1.48(0.03)	—	6322
1ES 0806+524	2.31(0.06)	1.80(0.02)	26(8)	1297
1ES 1011+496	7.6(0.1)	1.75(0.01)	33(5)	1066
Markarian 421	18.0(0.1)	1.73(0.005)	19(2)	1286
Markarian 180	0.164(0.008)	1.77(0.03)	—	2679
1ES 1215+303	9.04(0.14)	1.84(0.01)	44(5)	1066
1ES 1218+304	0.215(0.007)	1.69(0.02)	—	4442
PKS 1440-389	1.01(0.03)	1.70(0.03)	56(11)	2014
PG 1553+113	3.93(0.06)	1.56(0.01)	38(5)	1847
Markarian 501	4.57(0.07)	1.70(0.01)	17(4)	1478
1ES 1727+502	0.202(0.008)	1.75(0.03)	—	3005
1ES 1959+650	3.22(0.05)	1.76(0.01)	23(5)	1733
PKS 2005-489	0.526(0.016)	1.80(0.02)	—	2398
PKS 2155-304	15.4(0.2)	1.77(0.01)	35(3)	1136
1ES 2344+514	0.807(0.03)	1.73(0.03)	50(12)	1938

4.3 Parameter estimates: ALPs hypothesis

The alternative (H_1) hypothesis with photon-ALPs mixing includes two additional free parameters which relate to the strength B of the magnetic field and the distance s over which the photons can mix in the constant external magnetic field. For each pair of B , s , we maximize the likelihood L_{max}^1 (or minimize $\chi_{\text{w/ALP}}^2$). We carry out this procedure for a discrete set of pairs of B and s located on a logarithmic grid with (150×150) steps where $10^{-3}\mu\text{G} \leq B \leq 1\mu\text{G} - 10^3\mu\text{G}$ and $10^{-2}\text{kpc} - 1\text{kpc} \leq s \leq 10^3\text{kpc} - 10^4\text{kpc}$. Units!! The ranges are chosen such that the critical energy E_c could fall into the analyzed energy range, and to include the best-fitting parameters of (B, s) under the H_1 hypothesis. In case of multiple local maxima found, we choose the combination which minimizes the total energy present in the magnetic field given by $\propto s^3 B^2$. The same criterion is used for the grid with the χ^2 values.

In order to test the significance of the alternative hypothesis against the null hypothesis,

we introduce the test statistics (TS) based upon the likelihood ratio:

$$TS(B, s) = -2 \times (\ln(L_{max}^0) - \ln(L_{max}^1(B, s))). \quad (4.6)$$

For example, in the left panel of Fig. 1 (for figures of other sources see Figs. 10-27 in Appendix A) we show the resulting values of $TS(B, s)$ on the grid for Markarian 421 (Mkn 421).

The value of the TS varies in a characteristic way for different values of B and s . For small values of B and s , the two hypotheses are not distinguishable as the survival probability $p_{\gamma \rightarrow a}$ is too small in comparison with the measurement uncertainties. For high values of B and s a large part of the parameter space is excluded. Notably, a repetitive pattern of local maxima occurs which are aligned along increasing values of B and s . The local maxima correspond to the case where $s \cdot \Delta_{osc} > 2\pi$ and therefore multiple oscillations occur. For increasing values of B , the critical energy E_{crit} decreases therefore, a wider part of the energy spectrum is affected.

On the search grid, we locate the global maximum of $TS(\hat{B}, \hat{s}) = 18.5$ for $\hat{B} = 21.0$ nG and $\hat{s} = 216.4$ kpc (see Table 8 in Appendix A for global maxima of other sources), which is marked with a white triangle error bar. In this particular case, the global maximum (\hat{B}, \hat{s}) is located at a local maximum which corresponds to the parameters with the smallest value of $B^2 \cdot s^3$ which is proportional to the total energy required to build up the magnetic field.

We mark down the chosen local maximum $TS(\hat{B}_0, \hat{s}_0)$ with the smallest value of $B^2 \cdot s^3$, which in this case is identical with the global best-fitting results, and is shown as a black point error bar in Fig. 1.

In a consistent way, we obtain the best-fitting parameters for (\hat{B}_0, \hat{s}_0) of chosen local maxima under the ALP hypothesis for the remaining sources listed in Table 3.

Similar to the approach used for the TS defined by the likelihood ratio,

$$\Delta\chi^2 = \chi_{w/o\ ALP}^2 - \chi_{w/\ ALP}^2, \quad (4.7)$$

is also calculated for the same grid and the best-fitting parameters which maximise the $\Delta\chi^2$ are obtained⁶. As an example, the right panel of Fig. 1 shows the corresponding grid of $\Delta\chi^2$ values. When comparing the $\Delta\chi^2$ values on the same grid as the TS values, the same patterns emerge and similar best-fitting values for (\hat{B}, \hat{s}) are found, as well as the values for (\hat{B}_0, \hat{s}_0) . There are however some differences which relate to the fact that the $\Delta\chi^2$ method is based upon a coarser binning of the energy spectra and therefore the oscillation features remain in some cases under-sampled. In the same way, we have obtained the best-fitting combinations of (\hat{B}, \hat{s}) and (\hat{B}_0, \hat{s}_0) from the χ^2 fit which are listed in Tables 6 and 7 (in Appendix A) respectively.

The best-fitting distance \hat{s}_0 range from ≈ 0.1 kpc (1ES 1218+304) up to ≈ 262 kpc (Markarian 180). The bulk of the source spectra favor a conversion within a distance range of 1 kpc to 200 kpc with a magnetic field strength between 10 nG and 10 μ G.

As an illustration of the best-fitting SED for the two hypotheses, we show in Fig. 2, the observed SED data points of Mkn 421 (see Figs. 28-45 in Appendix A for other sources) together with the model curves. In the left panel, the SED data points are calculated with the likelihood binning while in the right figure, the SED points are calculated for a coarser binning. The best-fitting curve for the null hypothesis is shown as a green dashed line and is for both fitting methods very similar. For the case of photon-ALPs mixing, the resulting

⁶Note, the definition of $\Delta\chi^2$ and the sign is chosen such that we can use comparable value of $\Delta\chi^2$ and TS .

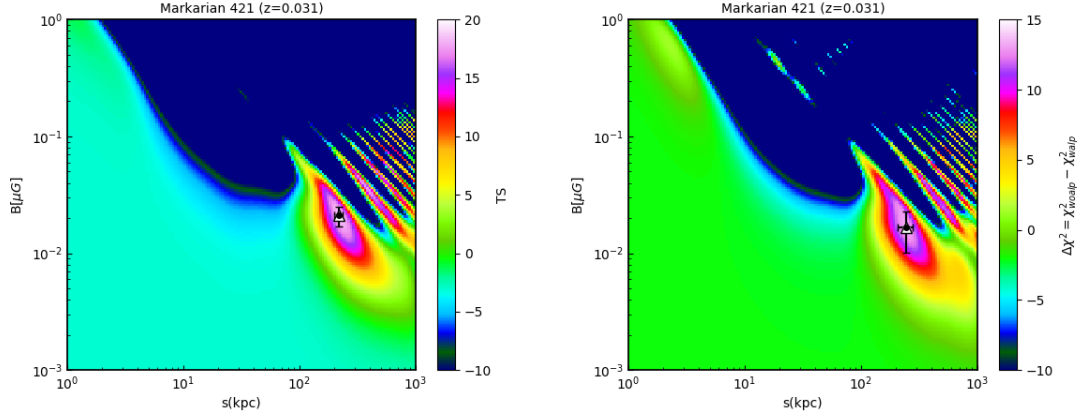


Figure 1. Left panel: (B, s) grid map where the color bar indicates the test statistics TS which is twice the difference of log-likelihood values between null and ALP hypotheses. Right panel: (B, s) grid map where the color bar indicates the difference of χ^2 values fitted in null and ALP hypotheses. The black and white marker correspond to the local and global best-fitting parameters respectively.

conversion probability leads to modifications of the spectrum mainly between 50 GeV and 500 GeV (shown as blue solid line). The relative amplitude of the modulation is about 15 %.

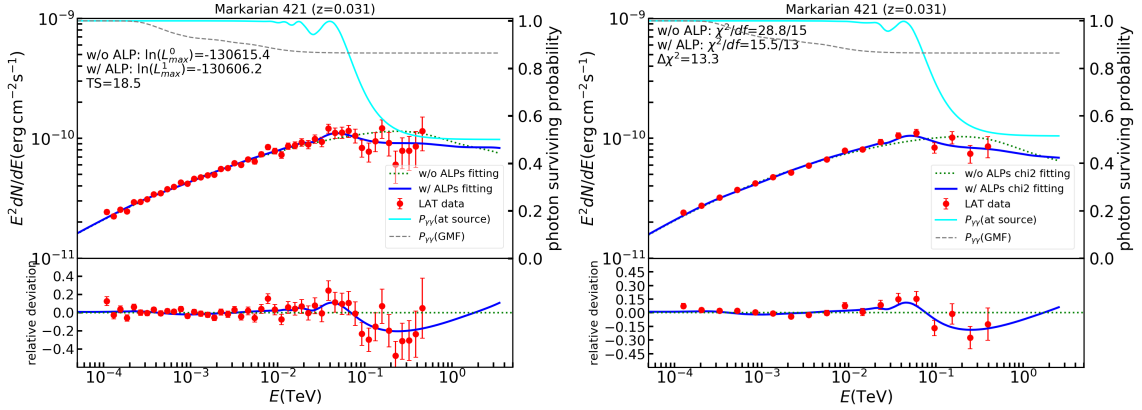


Figure 2. Left panel: the spectral energy distribution for source Mkn 421 with likelihood fitting method. The red data points are collected from a 10-yr LAT observation. The blue straight line is the best-fitting model with photon-ALP mixing effects included, and the green dashed line is the best-fitting model without the assumption of photon-ALP mixing. The cyan solid line is the photon surviving probability at source and the gray dashed line is the photon surviving probability at Milky Way. In the lower panel, we show the relative deviations of the flux points and “w/ ALP” scenario from the baseline (“w/o ALP”). Right panel: SED for source Mkn 421 with χ^2 fitting method.

4.4 Hypotheses testing for the joined *Fermi*-LAT spectra

The hypotheses testing is performed first on the individual energy spectra and subsequently in a analysis of the joined test statistics of all spectra.

Table 3. Best-fitting parameters of local maxima for ALP hypothesis with likelihood method using the modeled spectra from Eq. (4.4). B and s are additional free parameters relating to the strength and length scale for the external magnetic field that is responsible for photo-ALP mixing effects. The normalisation is given in units of $10^{-12}\text{MeV}^{-1}\text{cm}^{-2}\text{s}^{-1}$. Parameters uncertainties (1σ) are included.

AGN name	N_0	α	β $\times 10^{-3}$	E_b [MeV]	\hat{B}_0 [nG]	\hat{s}_0 [kpc]
1ES 0033+595	0.593(0.023)	1.54(0.03)	36(12)	3177	54.9 (27.9)	81.8 (28.4)
3C 66A	12.5(0.2)	1.80(0.01)	43(6)	1211	322.7 (46.1)	7.2 (0.9)
PKS 0301-243	10.4(2.8)	1.78(0.05)	41(10)	954.4	24396.3(7912.3)	0.2 (0.1)
NGC 1275	103(5)	1.99(0.01)	82(3)	883.6	26268.2(1142.6)	0.2 (0.01)
PKS 0447-439	7.20(0.14)	1.55(0.01)	87(6)	1605	1675.6(157.3)	2.0 (0.1)
1ES 0502+675	0.0731(0.0047)	1.49(0.03)	—	6322	820.5 (74.1)	12.2 (0.7)
1ES 0806+524	2.32(0.06)	1.78(0.02)	11(10)	1297	143.8 (21.2)	43.5 (3.8)
1ES 1011+496	7.67(0.12)	1.75(0.01)	25(6)	1066	27.1 (5.7)	206.2(24.1)
Markarian 421	19.1(0.2)	1.69(0.005)	13(2)	1286	21.0 (4.1)	216.4(18.4)
Markarian 180	0.177(0.008)	1.72(0.03)	—	2679	16.7 (11.9)	262.8(84.4)
1ES 1215+303	17.1(3.0)	1.77(0.06)	61(5)	1066	18574.9(4545.8)	0.3(0.1)
1ES 1218+304	0.426(0.015)	1.69(0.02)	—	4442	32031.9(7981.4)	0.1(0.04)
PKS 1440-389	1.76(0.09)	1.50(0.03)	105(12)	2014	2013.3(629.7)	2.2 (0.4)
PG 1553+113	4.96(0.10)	1.44(0.01)	43(6)	1847	846.0 (36.5)	11.1(0.3)
Markarian 501	7.88(1.40)	1.67(0.02)	24(4)	1478	29047.0(7747.1)	0.2(0.03)
1ES 1727+502	0.260(0.012)	1.72(0.02)	—	3005	1987.1(65.4)	9.3 (0.2)
1ES 1959+650	3.41(0.06)	1.71(0.01)	15(6)	1733	63.8 (29.5)	29.6 (8.1)
PKS 2005-489	0.707(0.048)	1.73(0.02)	—	2398	6400.6(374.4)	1.6 (0.1)
PKS 2155-304	30.8(0.3)	1.76(0.01)	42(3)	1136	30009.3(6113.0)	0.1(0.01)
1ES 2344+514	0.870(0.037)	1.62(0.04)	33(16)	1938	244.2 (71.1)	15.0 (2.9)

For either rejection or acceptance of null hypothesis, we estimate the distribution of TS under the null hypothesis following a similar procedure as described in [35]. We generate as pseudoexperiments (PE) 400 sets of simulated gamma-ray spectra for each source under the null hypothesis. The simulation of PE data sets is done through Gaussian sampling of the expected event numbers in a counts cube generated for the gamma-ray sources and diffuse emission present in the region of interest [36]. The resulting sim data sets are then subject to the same data analysis procedure as outlined above. For each source, this results in two distributions with 400 values of TS according to Eq. (4.6) and $\Delta\chi^2$ as defined in Eq. (4.7), respectively.

In the case of nested hypotheses the distribution of the test statistic should asymptotically approach a χ^2 distribution (in this case a non-central χ^2 distribution under null hypothesis) if the number of simulations is sufficiently high [39].

As an example, we present in Fig. 3 the distributions of TS for Mkn 421 with likelihood ratio test. The TS distribution is best approximated with a non-central χ^2 distribution (NCD) with about 0 degree of freedom (df) and non-centrality (nc) parameter $nc = 19.11$. With the accumulated NCD, we derive the probability to find a value of TS larger than the one found in data ($TS = 18.5$) to be $p(TS > 18.5; df = 0.00, nc = 19.11) = 2.79 \times 10^{-4}$, corresponding to a significance level of 3.6σ . The result on Mkn 421 for the χ^2 fit is slightly

less significant with $p(\Delta\chi^2 > 13.3; df = 4.38, nc = 9.82) = 7.39 \times 10^{-3}$, corresponding to a significance level of 2.7σ . Upon closer inspection, the binning for the χ^2 -fit is under-sampling the modulation predicted for the spectrum when photon-ALPs oscillation is considered. We can conclude from both tests, that in this case, the photon-ALP hypothesis is preferred over the null hypothesis.

The goodness of fit for the hypothesis H_1 is acceptable for 12 of the 20 spectra. Particularly, for 1ES 0502+675 and 1ES 1727+502, the resulting values of $\chi^2(df) = 38.2(14)$ and $\chi^2(df) = 32.7(14)$ are too large to be acceptable. The corresponding probability to obtain a larger value of χ^2 is $p(\chi^2 > 38.2, df = 14) = 4.8 \times 10^{-4}$ and $p(\chi^2 > 25.9, df = 14) = 3.2 \times 10^{-3}$, indicating a poor fit in both cases. Upon inspecting the SEDs and the residuals in Figs. 33 and 42, additional features in the spectrum are present which are not well described by the model.

Following the same approach, we present the obtained TS values for all the sources in Table 4, as well as their corresponding significance levels derived from null distribution for each source. As is evident from Table 4, the other sources show a similar preference for hypotheses H_1 with photon-ALPs mixing.

In order to test the overall preference of the joint data sets, we combine the TS for the individual sources:

$$TS_{\text{tot}} = \sum_i TS_i, \quad (4.8)$$

where TS_i is the test statistics for each individual source. Similarly, we combine the PE results from the individual sources in a bootstrapping approach. In order to do so, we take 10^7 sequences of 20 uniform random deviates n_1, \dots, n_{20} in order to combine the sources in a random way:

$$PE = \{(TS_{n_1}, \dots, TS_{n_{20}}) | n_1, \dots, n_{20} \in \{1, \dots, 400\}\}. \quad (4.9)$$

This way, we calculate a distribution of 10^7 values of TS^{PE} derived from the PE:

$$TS^{PE} = \sum_i TS_{n_i}. \quad (4.10)$$

With this approach we benefit from the combinatorial factor of $400^{20} \approx 10^{52}$ different possibilities to combine the simulated data sets. The combined analysis of the $\Delta\chi^2$ test is done in a similar way: we add up the individual $\Delta\chi^2$ values to obtain $\Delta\chi_{\text{tot}}^2$, and generate 10^7 values of $(\Delta\chi^2)^{PE}$ similar to the procedure outlined in Eqs. (4.9), (4.10).

The resulting distributions of TS^{PE} and $(\Delta\chi^2)^{PE}$ are shown in Fig. 4. The probability density function can be approximated by a NCD, similar to the distributions for the individual sources. The distribution of TS^{PE} is well fit by the NCD and the probability to find a value of $TS^{PE} > TS_{\text{tot}}$ can be estimated from the best-fitting NCD⁷ to be $p(TS^{PE} > TS_{\text{tot}} = 98.9; df = 140.20, nc = 162.49) = 1.22 \times 10^{-7}$, corresponding to a z -score of 5.3. For the $\Delta\chi^2$ based hypotheses test, we find the NCD fit a poor description of the underlying simulated distribution for small values of $\Delta\chi^2$. For larger values of $\Delta\chi^2$ the fit matches closely the distribution. We estimate the z -score to be smaller than the value found for the TS -based distribution at 1.4. This is consistent with the findings from the individual sources.

⁷A similar value is obtained by counting the number of entries in the simulated distribution with $TS^{PE} > TS_{\text{tot}}$.

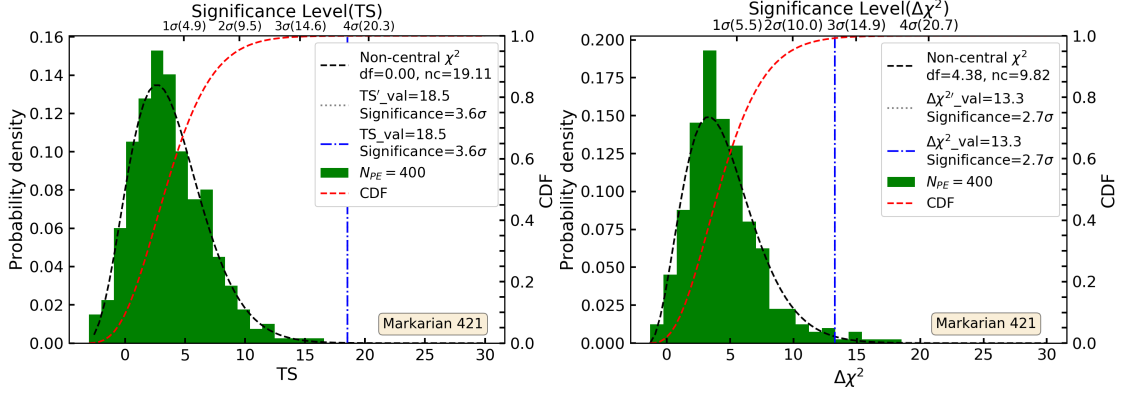


Figure 3. Left panel: Simulated null distribution for Mrk 421 from likelihood ratio test. Right panel: Simulated null distribution from $\Delta\chi^2$ test for the same source. The black dashed line indicates a fit to the distribution with a non-central χ^2 function. The red solid line represents the resulting cumulative distribution function (CDF). The $TS(\Delta\chi^2)$ value derived from the local maxima of original data is marked as a blue (dot-dash) vertical line, while the $TS(\Delta\chi^2)$ value obtained from the global maxima is marked as a gray dotted line (in this case, the blue line coincides with the gray line).

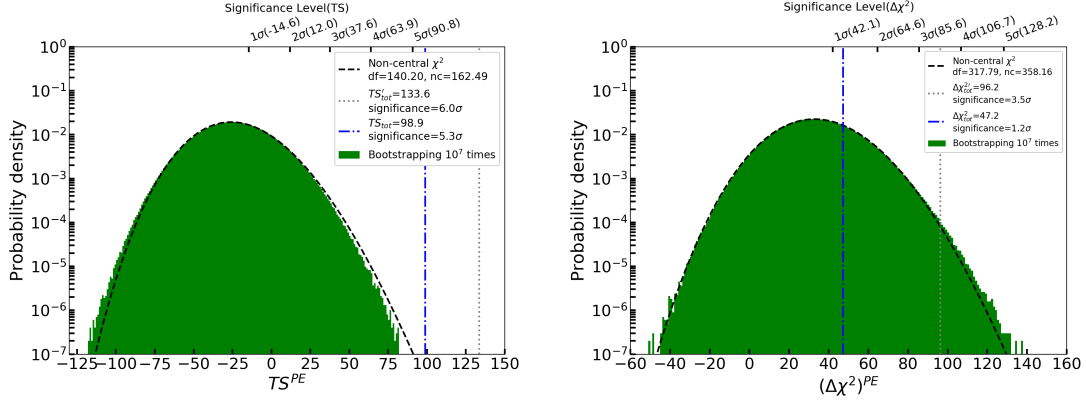


Figure 4. Left panel: Combined full null TS distribution from likelihood ratio test using bootstrapping method. Right panel: Combined full null $\Delta\chi^2$ distribution from $\Delta\chi^2$ test using bootstrapping method. Black dashed line denotes fitting to the histogram of $TS^{PE}((\Delta\chi^2)^{PE})$ values with non-central χ^2 (NCD) function. Blue dotted-dash line indicates the position of $TS_{tot}(\Delta\chi_{tot}^2)$. Gray dotted line stands for the position of $TS'_{tot}(\Delta\chi_{tot}^2)$ summed over all global maximal values on (B, s) grid maps (see App. A the white triangle on each grid map).

4.5 Combined HE and VHE spectra

The large collection area of ground-based instruments extends the high energy (HE) range accessible with *Fermi*-LAT towards very high energies (VHE), where photon statistics limit the sensitivity for space based instruments. The downside of the ground-based technique is a limited field of view. Therefore, the VHE spectrum is in most cases recorded during flaring states whereas the HE spectrum is recorded quasi-continuously with the all-sky instrument of *Fermi*-LAT. The flare-selected observation of AGN with ground based instruments introduces a bias in the observed energy spectrum towards a high flux-state which is not necessarily representative of a truly time-averaged spectrum.

Table 4. Best-fitting log-likelihood and χ^2 values of the local maxima for null (H_0) and ALP hypotheses (H_1). TS values are calculated with Eqs. (4.6) and (4.7) for likelihood ratio test and $\Delta\chi^2$ test respectively. Corresponding significance levels for both tests are listed as well.

AGN name	H_0 $\ln(L_{max}^0)$	H_1 $\ln(L_{max}^1)$	TS	z -score (H_1/H_0)	H_0 $\chi^2_{w/o\ ALP}/df$	H_1 $\chi^2_{w/ALP}/df$	$\Delta\chi^2$	z -score (H_1/H_0)
1ES 0033+595	712253.0	712257.2	8.4	2.1	22.2/15	14.2/13	8.1	1.9
3C 66A	-122858.4	-122856.5	3.8	2.0	20.6/15	16.3/13	4.3	2.3
PKS 0301-243	-154508.6	-154508.2	0.7	0.5	16.3/15	16.4/13	-0.2	0.5
NGC 1275	26767.7	26777.6	19.8	3.6	25.6/15	22.6/13	3.1	1.8
PKS 0447-439	-146200.2	-146199.2	2.0	1.9	26.2/15	25.8/13	0.4	1.5
1ES 0502+675	-44659.7	-44656.4	6.7	1.3	41.9/16	38.2/14	3.6	0.4
1ES 0806+524	-159751.7	-159750.4	2.6	0.2	20.5/15	16.6/13	3.9	0.5
1ES 1011+496	-153504.9	-153502.4	5.0	0.8	12.7/15	9.2/13	3.5	0.4
Markarian 421								
10yrs LAT	-130615.4	-130606.2	18.5	3.6	28.8/15	15.5/13	13.3	2.7
simul. LAT+MAGIC	—	—	—	—	33.4/15	20.7/13	12.6	1.8
Markarian 180	-132628.5	-132627.9	1.0	0.01	23.8/16	20.5/14	3.3	0.4
1ES 1215+303	-143988.2	-143984.9	6.6	2.0	15.5/15	13.4/13	2.1	1.2
1ES 1218+304	-145577.4	-145577.9	-1.0	0.9	19.0/16	20.2/14	-1.2	1.1
PKS 1440-389	60781.3	60783.1	3.7	1.3	18.9/15	17.0/13	3.5	0.6
PG 1553+113	-152448.4	-152450.6	-4.2	0.02	17.8/15	27.7/13	-9.9	0.0
Markarian 501	-95747.1	-95746.2	1.7	0.4	18.5/15	17.2/13	1.4	0.3
1ES 1727+502	-154208.5	-154207.4	2.4	0.4	26.7/16	32.7/14	-6.1	0.0
1ES 1959+650	-49456.2	-49453.9	4.6	0.7	21.6/15	16.3/13	5.3	0.9
PKS 2005-489	-166314.9	-166309.0	11.4	2.1	33.9/16	20.9/14	12.9	2.1
PKS 2155-304								
10yrs LAT	-144503.6	-144503.1	0.9	1.5	15.8/15	19.5/13	-3.6	0.5
simul. LAT+H.E.S.S.	—	—	—	—	33.3/18	29.2/16	4.1	1.6
1ES 2344+514	-61475.6	-61472.2	6.7	1.2	15.2/15	14.0/13	1.2	0.5

In the following, we consider examples for the combination of HE and VHE data taken from PKS 2155-304 ($z = 0.116$) and Mkn 421 ($z = 0.031$), where HE and VHE data are recorded contemporaneously with *Fermi*-LAT and ground-based instruments.

4.5.1 Combined spectrum of PKS 2155-304

The nearby X-ray selected AGN PKS 2155-304 is the first extra-galactic very high energy gamma-ray source discovered in the southern sky [40]. It has been closely monitored, both during periods of quiescence as well as during flares [41].

We consider a quasi-simultaneous observation to avoid the combination of data sets averaged over different flux states. Non-simultaneous spectral data could lead to an apparent spectral break or irregularities close to the transition energy of the two measurements. The constraint on available contemporaneous observation time leads to larger statistical uncertainties on the detected photon numbers which in turn reduce the sensitivity for spectral features. During contemporaneous observations of PKS 2155-304 with H.E.S.S.-II and *Fermi*-LAT in 2013, a spectral break between the HE and VHE data is observed [42]. The H.E.S.S. Phase II observations achieved a reduced energy threshold in comparison with the previous measurements recorded with the smaller H.E.S.S. Phase I instruments [41]. The

lower threshold of H.E.S.S. II observations improves the overlap in the energy range covered with space and ground based instruments. We re-analyse the contemporaneous *Fermi*-LAT data set used by [42] with identical energy bins to combine the two measurements.

We present in Fig. 5 the scan of $\Delta\chi^2(B, s)$ from the combined energy spectrum for the ALP hypothesis H_1 . The global best-fitting parameters are found to be at $\hat{B} = 5.5 \mu G$, with $\hat{s} = 0.2$ kpc, where $\Delta\chi^2 = 4.1$ is obtained. As can be seen from Fig. 5, the local maximum (\hat{B}_0, \hat{s}_0) (indicated with a black point) coincides with the global maximum (indicated with a white triangle).

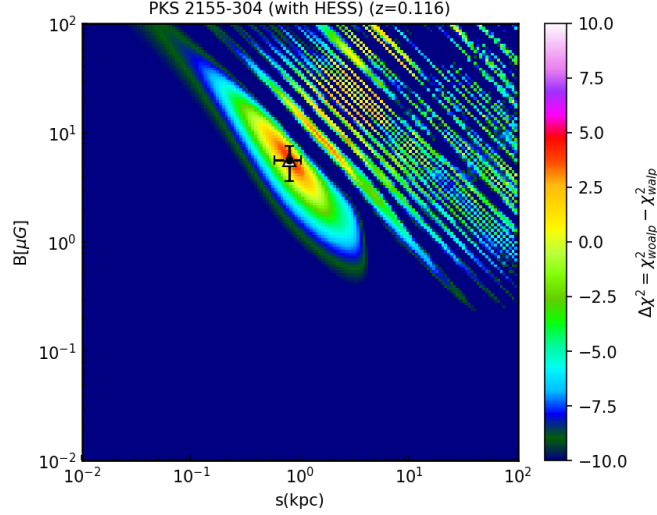


Figure 5. $\Delta\chi^2$ for a grid of values of B-field strength B and distance s . The color bar indicates the $\Delta\chi^2$ values when fitting the combined contemporaneous LAT and H.E.S.S. data in 2013. The black point marker indicates the local maximum of $\Delta\chi^2$ derived from the fit of the SED to the combined spectrum, while the white triangle marker represents the global best-fitting parameters.

The resulting spectral energy distribution is shown in Fig. 6. The spectral break is observed at an energy of (48 ± 12) GeV when fitting a broken-power law to the combined SED. The flux measurements in the overlapping energy range between 80 GeV and 300 GeV are consistent between the two instruments. The H_0 hypothesis is not providing a good description of the data while the H_1 hypothesis improves slightly the fit by $\Delta\chi^2 = 4.1$. Using mock data sets, we estimate the significance in a similar way as before. The resulting distribution for $\Delta\chi^2$ and a NCD fit function is shown in Fig. 6 (right panel). The z-score for the improvement is estimated to be ≈ 1.6 .

4.5.2 Combined spectrum from Mkn 421

The northern, nearby AGN Mkn 421 ($z = 0.031$) is a highly variable BL Lac type object that has been closely monitored since the discovery of its VHE emission [43]. While a number of simultaneous multi-wavelength observations have been carried out for this source, we select the result reported by [44] on a simultaneous observation campaign with *Fermi*-LAT and the MAGIC telescopes from January to June 2009. During this campaign, the combined energy spectrum from the two instruments covers a very broad energy range with substantial overlap between the two instruments.

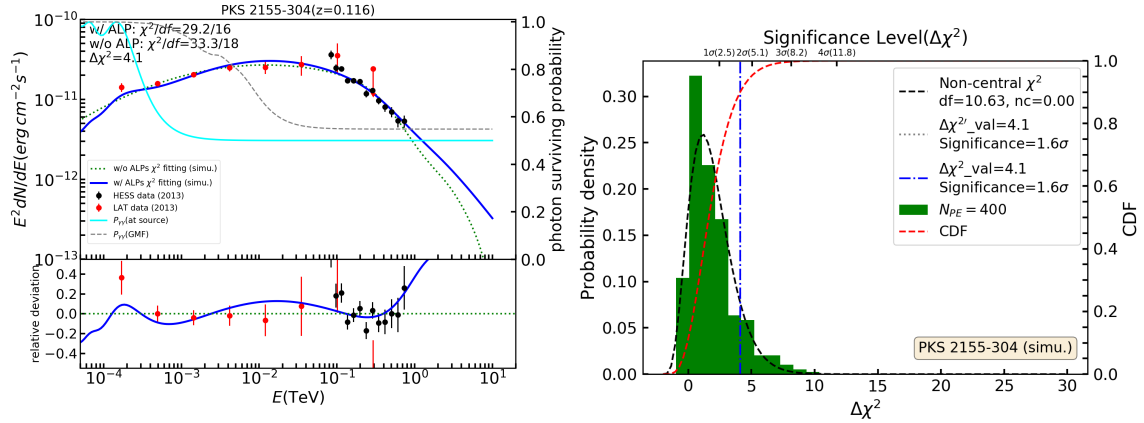


Figure 6. Left panel: the spectral energy distribution for PKS 2155-304 during contemporaneous observations with H.E.S.S.-II and *Fermi*-LAT in 2013. The red data points represent the 2013 LAT observations, and the black data points are from H.E.S.S. during the same year. The blue solid and green dashed lines are the best-fitting models under H_0 and H_1 hypotheses respectively. The cyan solid and gray dashed lines stand for the photon surviving probabilities in different regions along the line of sight. Right panel: simulated null distribution from $\Delta\chi^2$ test for 2013 H.E.S.S. and LAT observations. The black dashed line indicates a fit to the distribution with a non-central χ^2 function. The red solid line represents the resulting cumulative distribution function (CDF). The $\Delta\chi^2$ value derived from the original data is marked as a blue (dot-dash) vertical line.

The scan of the parameters s and B for the combined spectrum shows several maxima which would favor either a large magnetic field of several μG on kpc scales or a very weak magnetic field of several nG over Mpc distances (see Fig. 7). The chosen the local maximum, corresponding to a minimum energy, is marked with a black cross in Fig. 7 where the resulting critical energy ≈ 100 MeV (see Eq. (2.10)).

The SED for Mkn 421 is obtained by reanalysing *Fermi*-LAT data from the observation season covered with MAGIC from January to June 2009 [44]. The resulting SED is displayed in Fig. 8. The spectrum shows a softening just below TeV energies, deviating noticeably from the log-parabola shape (green dashed line in Fig. 8). The fit under the alternative H_1 hypothesis improves the goodness of fit by $\Delta\chi^2 = 12.6$ such that the resulting $\chi^2_{H1} = 20.7$ for 13 degrees of freedom. This value is slightly larger than expected due to two flux points between 100 and 200 GeV which deviate by more than two standard deviations from the fit.

The z-score of the improvement is estimated to be 1.8 (see Fig. 8, right panel).

5 Discussion

The search for spectral modulations in extra-galactic energy spectra has been carried out for 20 objects that have been selected to provide an optimized coverage in energy. For 18 sources (see Table 4), the fits show a consistent improvement when including a photon-ALPs conversion (hypothesis H_1) in comparison to the null hypothesis (H_0). When inspecting the individual spectra (see Figs. 28-45), the photon-ALPs conversion in the GMF and the magnetic field intrinsic to the source leads to a rich phenomenology of spectral shapes. The resulting breaks, dips, and bumps occur predominantly at the critical energy (see Eq. 2.10) specific to the GMF and the source-intrinsic magnetic field.

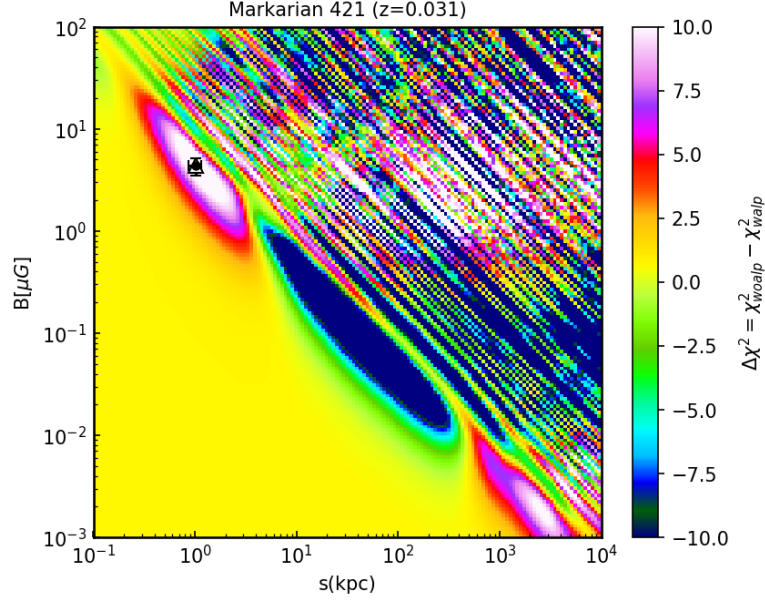


Figure 7. $\Delta\chi^2$ distribution as functions of B-field strength B and distance s . The color bar indicates the $\Delta\chi^2$ values when fitting the combined time-averaged LAT and MAGIC data [44]. The black point marker indicates the local maximum of $\Delta\chi^2$ derived from the fit of the SED to the time averaged spectrum, while the white triangle marker stands for the global maximum of $\Delta\chi^2$.

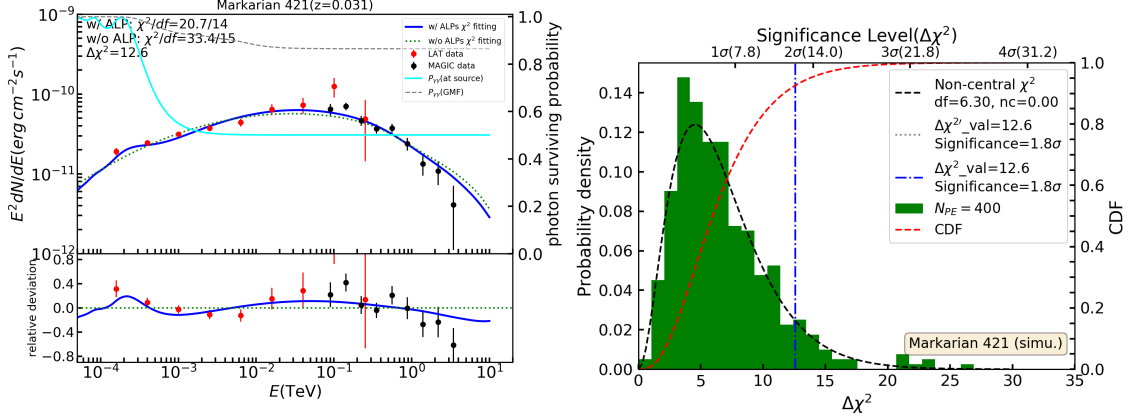


Figure 8. Left panel: the spectral energy distribution for Markarian 421 during contemporaneous observations with MAGIC and *Fermi*-LAT in 2009. The red data points represent the 2009 LAT observations, and the black data points are from MAGIC [44] during the same year. The blue solid and green dashed lines are the best-fitting models under H_0 and H_1 hypotheses respectively. The cyan solid and gray dashed lines stand for the photon surviving probabilities in different regions along the line of sight. Right panel: simulated null distribution from $\Delta\chi^2$ test for 2009 MAGIC and LAT observations. The black dashed line indicates a fit to the distribution with a non-central χ^2 function. The red solid line represents the resulting cumulative distribution function (CDF). The $\Delta\chi^2$ value derived from the original data is marked as a blue (dot-dash) vertical line.

The most significant improvement can be seen as expected in the spectra which have the largest signal-to-noise ratio, i.e. Mkn 421 (Fig. 2) with $TS = 18.5$ and NGC1275 (Fig. 31) with $TS = 19.8$. Another source with a well-measured spectrum is PG 1553+113 (Fig. 40). The spectrum has apparently several features that are not predicted in our model. Subsequently, the resulting $TS = -4.2$ would favor the H_0 hypothesis. However, the source could be embedded in a cluster environment where weak mixing in the turbulent magnetic field provides a better description of the observed spectrum.

The findings obtained with the likelihood-method have been largely confirmed when fitting the SED with a χ^2 -based approach. The wider binning leads to an under-sampling of the spectral features that are visible in the spectra obtained for the likelihood analysis. The resulting significance in the χ^2 -based approach is therefore smaller than for the likelihood approach. The χ^2 -based approach is however useful when combining data sets from *Fermi*-LAT with ground-based measurements. We have demonstrated that for contemporaneous data-sets on PKS2155-304 and Mkn 421, the energy range can be extended in a meaningful way. However, no additional features are observed in the wider energy range. In the case of PKS 2155-304, the re-conversion of ALPs leads to an enhanced flux at energies exceeding a few TeV which is slightly favored by the data.

The combination of the results obtained with the relevant likelihood-analysis has been carried out for all 20 sources. When combining the likelihood results for the local maxima in the B - s plane, we find a total TS value of $TS_{\text{tot}} = 98.9$. The local maxima is chosen to minimize the energy requirement to sustain a magnetic field with energy density $\propto B^2$ over a volume $\propto s^3$. This is considerably smaller than the value found when combining the global maxima of all sources with $TS'_{\text{tot}} = 133.6$.

A bootstrap-type combination of the same analyses carried out on mock data-sets that have been simulated under the null hypothesis are used to estimate the significance. We estimate the chance probability to find a TS_{tot} value larger than 98.9 to be 1.2×10^{-7} corresponding to a significance of 5.3σ . For the global maximum, the estimated significance reaches 6σ .

The required values of average transversal magnetic field \hat{B}_0 and extension \hat{s}_0 found for the individual sources fall into a wide range covering several orders of magnitude as shown in Fig. 9.

We compare in the same figure the values found in the fitting procedure with the range of values for magnetic fields possibly present in the vicinity of the considered sources. This includes the magnetic field in the outer regions of the jet (lobes) [45–47] as well as the magnetic field present in the host galaxy. In the wider vicinity of the source, we can expect that some objects are located in galaxy groups or galaxy clusters which are known to support an intra-cluster magnetic field (ICMF) with a turbulent and large scale component [16, 33–35, 48–52]. Recently, low-frequency radio-observations have revealed the presence of a large-scale magnetic field in the circumgalactic medium (CGM) [53].

Finally, the IGMF in filaments [54–60] along the line of sight could contribute additional conversion regions. The IGMF [30] in voids, however, is not relevant.

We note that the estimated values for \hat{B} and \hat{s} found for the 20 sources are nicely aligned with the astrophysically known magnetic fields. There is a noticeable cluster of six sources with $B = 20 \mu\text{G} - 30 \mu\text{G}$ for a spatial scale between $150 \text{ pc} - 300 \text{ pc}$. Similar large-scale fields are present in the central 200 pc of the Milky Way (galactic center field, GCF) [61], suggesting that the photon-ALPs conversion takes place in a similar environment in these sources.

In addition, we also indicate the prediction for formation of magnetic fields from magnetohydrodynamical simulation [62, 63]⁸. The result of the simulation traces well the observed values indicated in Fig. 9.

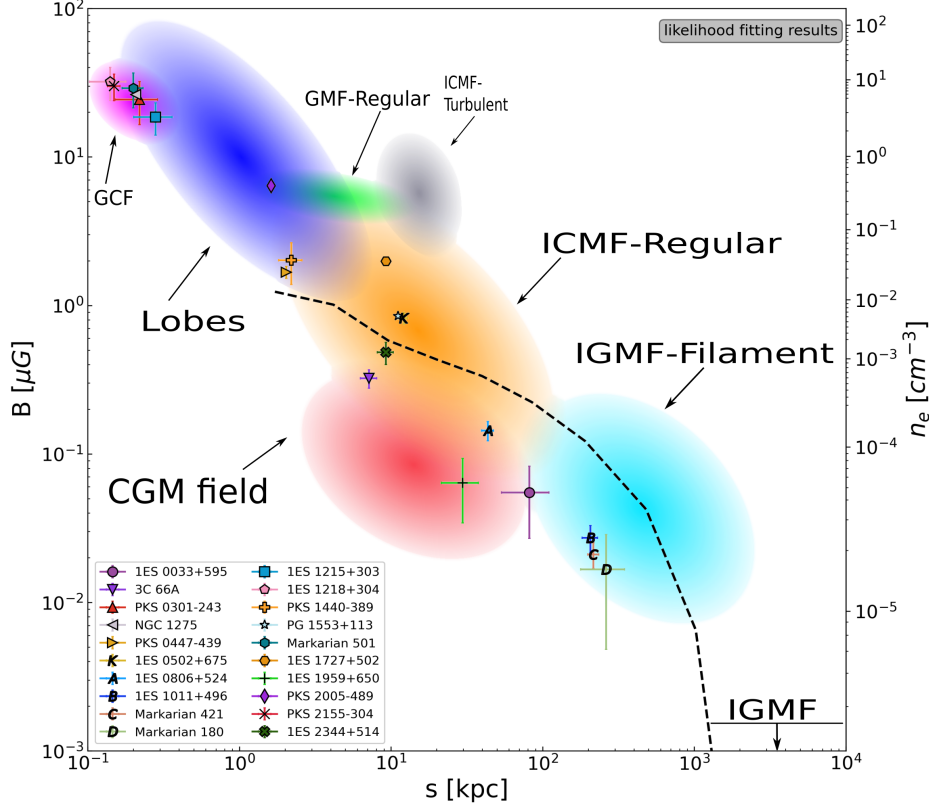


Figure 9. Likelihood best-fitting results of (\hat{B}_0, \hat{s}_0) from Table 3: The black dashed line is the cosmological magnetohydrodynamical simulation for radio haloes and magnetic fields in galaxy clusters which relate to the average electron density n_e [62, 63].

The result obtained here have been found under the assumption of fixed values for mass $m_a = 3.6$ neV and coupling $g_{a\gamma\gamma} = 2.3 \times 10^{-10} \text{ GeV}^{-1}$ [17], that are not consistent with the bounds provided by CAST [21] (see however Ref. [64] for a consistent interpretation of the two results). It is important to note, that the features visible in the energy spectra can also be fit with values for the coupling consistent with the bound from CAST ($g_{a\gamma\gamma} < 6.6 \times 10^{-11} \text{ GeV}^{-1}$, 95 % c.l.). In this case, the product of required magnetic field and length scale would need to be increased by a factor of ≈ 4 , which would not lead to unreasonable values of these parameters. However, more recent constraints for $g_{a\gamma\gamma} < 5.4 \times 10^{-12} \text{ GeV}^{-1}$ (95 % c.l.) have been derived from a re-analysis of the polarization from magnetized white dwarfs [65]. In this case, the necessary increase of the product of B and s to be ≈ 40 would push the best-fitting values to the upper end of astrophysically motivated values (see Fig. 9).

⁸The converted B-field values shown here are from Illustris TNG-300 simulation setup in Ref. [62]

6 Summary

- The fits to high-energy spectra of 20 extra-galactic gamma-ray sources improves significantly with $5.3(6.0)\sigma$ when including photon-ALPs mixing in a homogeneous magnetic field $\hat{B}_0(\hat{B})$ with spatial extension $\hat{s}_0(\hat{s})$ left free to vary for a fixed m_a and $g_{a\gamma\gamma}$. The values \hat{s}_0 , \hat{B}_0 relate to the local maximum in the TS with the additional condition that the total energy in the magnetic field $\propto \hat{B}_0^2 \hat{s}_0^3$ is minimized. The value in the parentheses corresponds to the global maximum.
- The individual sources with strong indications for additional spectral features present in the *Fermi*-LAT data are NGC1275 with $3.6(3.6)\sigma$ and Mkn 421 with also $3.6(3.6)\sigma$.
- The range of values found for \hat{B}_0 is consistent with expected and plausible values for the magnetic field strength found in astrophysical environments characterized by the length scales of \hat{s}_0 from several 100 pc to several 100 kpc (see Fig. 9).
- The observations of spectral modulations in AGN establish the disappearance channel of photon-ALPs mixing which is complementary to the appearance channel (anomalous transparency) that has provided the first indications for photon-ALPs mixing in gamma-ray spectra.
- The result shown here is degenerate for choosing a particular combination of coupling $g_{a\gamma\gamma}$ and mass m_a to achieve the required conversion probability $p_{\gamma\rightarrow a} \propto g_{a\gamma\gamma}^2 B^2 s^2$ above the critical energy $E_c \propto m_a^2/(g_{a\gamma\gamma} B)$. In this regards, the result presented here remains valid for different choices of $g_{a\gamma\gamma}$ and m_a which would be consistent with other exclusion limits and astrophysical expectations for magnetic field strength.

Acknowledgments

Part of this work has made use of data and software provided by the Fermi Science Support Center. Q.Y. acknowledges the support from China Scholarship Council and the Deutsche Forschungsgemeinschaft (DFG, German Research Foundation) under Germany's Excellence Strategy – EXC 2121 “Quantum Universe” – 390833306.

A Additional fit-results

In Table 5 we list the best-fitting parameters estimated using the χ^2 -minimization under the null-hypothesis (see Table 2 for the corresponding likelihood-fit results). The fit-results obtained with the χ^2 -method under the alternative hypothesis and evaluated at the local minimum are listed in Table 6 (see Table 3 for the likelihood-fit results). In Tables 7 and 8 we present the global best-fitting parameters with the χ^2 and likelihood methods respectively (supplementary to the information presented in Table 9). Finally, the Table 9 summarizes the result of the hypotheses tests when considering the global extrema (compare with Table 4 for the local extrema).

In the following figures (Figs. 10 to 27) we present the (B, s) grid maps with likelihood and χ^2 fitting for the sources in our sample collection. The corresponding best-fitting spectral energy distributions are provided in Figs. 28 to 45.

Table 5. Best-fitting parameters for the null hypothesis with the χ^2 method using the modeled spectra from Eq. (4.3). The estimated uncertainties (1σ) for each fitting parameters are listed as well. The value of $E_b = 10^5$ MeV is fixed, the normalisation is given in units of $10^{-15} \text{MeV}^{-1} \text{cm}^{-2} \text{s}^{-1}$.

AGN name	N_0	α	β $\times 10^{-3}$
1ES 0033+595	0.983(0.115)	1.71(0.08)	1(13)
3C 66A	1.10(0.09)	2.28(0.04)	45(5)
PKS 0301-243	0.509(0.064)	2.17(0.06)	36(8)
NGC 1275	0.802(0.046)	2.70(0.02)	70(3)
PKS 0447-439	1.29(0.10)	2.20(0.04)	55(5)
1ES 0502+675	0.86(0.07)	2.50(0.03)	—
1ES 0806+524	0.46(0.05)	2.11(0.06)	33(8)
1ES 1011+496	1.15(0.09)	2.06(0.04)	32(5)
Markarian 421			
10yrs LAT	6.34(0.20)	1.92(0.02)	22(2)
simul. LAT+MAGIC	3.28(0.18)	2.12(0.02)	50(5)
Markarian 180	0.226(0.026)	2.19(0.03)	—
1ES 1215+303	0.772(0.069)	2.28(0.04)	48(5)
1ES 1218+304	1.02(0.07)	2.29(0.02)	—
PKS 1440-389	0.484(0.06)	2.20(0.07)	63(11)
PG 1553+113	3.96(0.21)	1.87(0.03)	37(5)
Markarian 501	2.41(0.13)	1.86(0.03)	17(4)
1ES 1727+502	0.344(0.033)	2.20(0.02)	—
1ES 1959+650	1.60(0.11)	1.98(0.04)	26(5)
PKS 2005-489	0.572(0.043)	2.18(0.02)	—
PKS 2155-304			
10yrs LAT	2.44(0.13)	2.13(0.03)	40(3)
simul. LAT+H.E.S.S.	1.32(0.04)	2.22(0.03)	53(7)
1ES 2344+514	0.321(0.06)	2.23(0.11)	61(16)

Table 6. Best-fitting parameters of local maxima for ALP hypothesis with χ^2 method. Parameters uncertainties (1σ) are included. The value of $E_b = 10^5$ MeV is fixed, the normalisation is given in units of $10^{-15}\text{MeV}^{-1}\text{cm}^{-2}\text{s}^{-1}$.

AGN name	N_0	α	β $\times 10^{-3}$	\hat{B}_0 [nG]	\hat{s}_0 [kpc]
1ES 0033+595	1.74(0.20)	1.78(0.08)	188(12)	7547.5(3281.5)	1.5(0.6)
3C 66A	1.89(0.26)	2.20(0.05)	46(5)	374.7(62.6)	6.9(0.8)
PKS 0301-243	0.950(0.145)	2.18(0.12)	46(13)	21672.5(2918.8)	0.3(0.01)
NGC 1275	1.47(0.02)	2.74(0.01)	76(1)	39621.7(317.6)	0.1(1.6)
PKS 0447-439	2.46(0.22)	2.30(0.07)	909	1731.8(283.0)	2.0(0.2)
1ES 0502+675	1.35(0.21)	2.59(0.05)	—	104.4(54.0)	53.5(17.4)
1ES 0806+524	0.581(0.075)	2.00(0.07)	21(9)	25.5(10.2)	202.6(36.2)
1ES 1011+496	1.42(0.14)	1.98(0.05)	24(6)	35.7(7.3)	170.5(17.0)
Markarian 421					
10yrs LAT	8.71(0.43)	1.84(0.02)	16(3)	16.5(6.4)	242.0(35.1)
simul. LAT+MAGIC	7.25(0.37)	2.15(0.02)	71(5)	4344.2(845.6)	1.0(0.1)
Markarian 180	0.308(0.040)	2.25(0.03)	—	20.2(11.0)	226.2(72.9)
1ES 1215+303	1.44(0.16)	2.36(0.07)	69(12)	7385.9(5817.8)	0.4(0.3)
1ES 1218+304	1.98(0.14)	2.29(0.02)	—	295842.8(65007.2)	0.0(0.01)
PKS 1440-389	0.859(0.121)	2.38(0.08)	110(12)	2326.0(1404.3)	1.9(0.5)
PG 1553+113	7.40(0.40)	1.78(0.04)	40(5)	840.1(88.9)	10.9(1.0)
Markarian 501	4.07(0.38)	1.87(0.02)	24(3)	29607.5(3114.0)	0.2(0.02)
1ES 1727+502	0.479(0.044)	2.23(0.02)	—	1355.6(341.8)	6.8(1.3)
1ES 1959+650	2.33(0.31)	1.89(0.05)	22(5)	137.7(67.8)	11.1(3.4)
PKS 2005-489	1.01(0.09)	2.24(0.02)	—	8025.7(2126.2)	1.3(0.3)
PKS 2155-304					
10yrs LAT	4.69(0.24)	2.16(0.03)	43(3)	60241.1(10007.3)	0.1(0.01)
simul. LAT+H.E.S.S.	2.69(0.09)	2.34(0.02)	86(7)	5589.7(1975.4)	0.8(0.2)
1ES 2344+514	0.731(0.132)	2.15(0.12)	75(17)	619.9(204.6)	7.5(1.5)

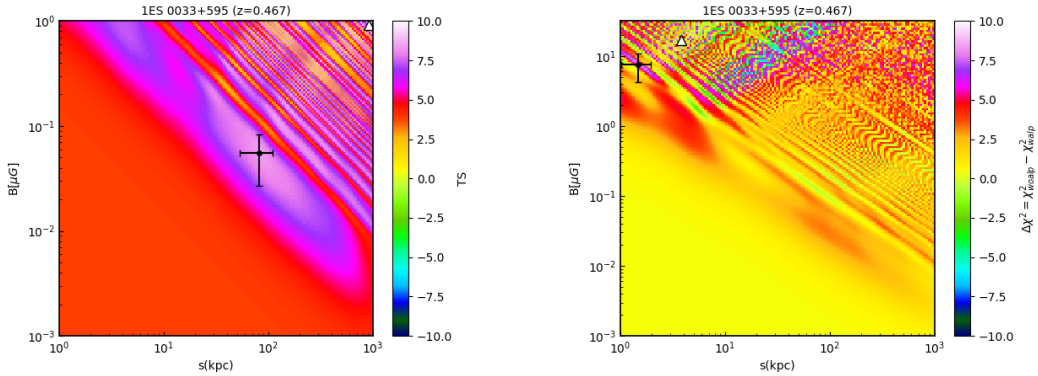


Figure 10. 1ES 0033+595, same as Fig. 1.

Table 7. Best-fitting parameters for ALP hypothesis with χ^2 method using the modeled spectra from Eq. (4.4). Parameters uncertainties (1σ) are included. The value of $E_b = 10^5$ MeV is fixed, the normalisation is given in units of $10^{-15}\text{MeV}^{-1}\text{cm}^{-2}\text{s}^{-1}$.

AGN name	N_0	α	β $\times 10^{-3}$	\tilde{B} [nG]	\hat{s} [kpc]
1ES 0033+595	1.77(0.20)	1.75(0.08)	13(13)	17047.7(2689.8)	3.8(0.6)
3C 66A	1.89(0.26)	2.20(0.05)	46(5)	374.8(62.6)	6.9(0.8)
PKS 0301-243	0.955(0.078)	2.17(0.05)	46(5)	88403.9(532.1)	1.8(0.01)
NGC 1275	1.43(0.13)	2.75(0.03)	78(4)	33752.1(9973.8)	0.1(0.03)
PKS 0447-439	2.50(0.19)	2.23(0.04)	74(6)	8922.0(54.8)	57.7(0.4)
1ES 0502+675	1.42(0.17)	2.57(0.03)	—	910.7(6.9)	272.8(1.8)
1ES 0806+524	0.617(0.085)	1.98(0.07)	19(10)	51.8(7.6)	278.5(28.4)
1ES 1011+496	1.79(0.16)	1.89(0.04)	16(6)	120.9(1.6)	855.7(8.9)
Markarian 421					
10yrs LAT	8.71(0.44)	1.84(0.02)	16(3)	16.5(6.6)	242.2(37.4)
simul. LAT+MAGIC	7.25(0.37)	2.15(0.02)	71(5)	4344.2(845.6)	1.0(0.1)
1ES 1215+303	1.44(0.16)	2.36(0.07)	69(12)	7392.7(5743.8)	0.4(0.3)
1ES 1218+304	2.00(0.14)	2.30(0.02)	—	308906.8(516.5)	7.3(0.01)
PKS 1440-389	0.931(0.119)	2.28(0.08)	91(12)	30894.1(26.7)	200.5(0.2)
PG 1553+113	7.29(0.16)	1.88(0.01)	53(1)	2647.4(0.0)	226832.3(0.4)
Markarian 501	4.40(0.25)	1.85(0.03)	15(5)	59644.3(1303.1)	2.5(0.1)
1ES 1727+502	0.446(0.042)	2.18(0.02)	—	61936.7(16.3)	395.7(0.1)
1ES 1959+650	2.75(0.29)	1.81(0.05)	13(7)	180.6(1.8)	627.7(3.5)
PKS 2005-489	0.895(0.076)	2.22(0.02)	—	11432.8(151.3)	20.4(0.3)
PKS 2155-304					
10yrs LAT	4.51(0.24)	2.11(0.03)	49(4)	4912.4(1.4)	925.6(0.2)
simul. LAT+H.E.S.S.	2.69(0.09)	2.34(0.02)	86(7)	5589.7(1975.4)	0.8(0.2)
1ES 2344+514	0.690(0.152)	2.21(0.12)	83(17)	1159.7(390.0)	11.9(3.3)

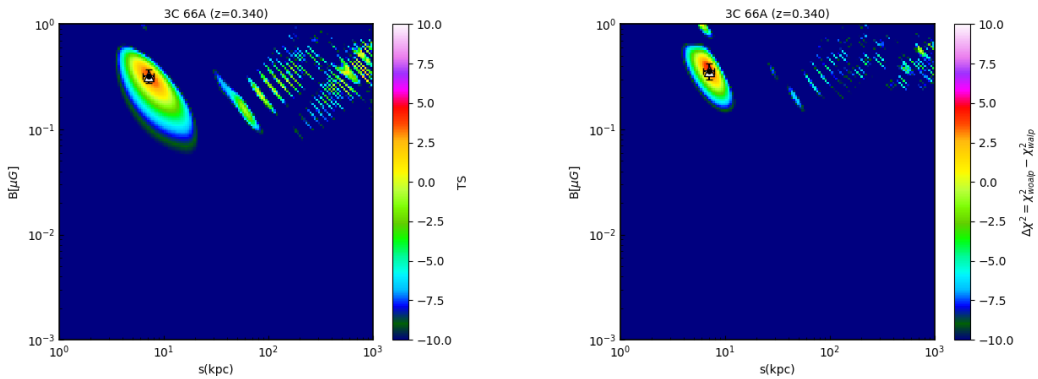


Figure 11. 3C 66A, same as Fig. 1.

Table 8. Best-fitting parameters for ALP hypothesis with likelihood method using the modeled spectra from Eq. (4.4). The normalisation is given in units of $10^{-12}\text{MeV}^{-1}\text{cm}^{-2}\text{s}^{-1}$. Parameters uncertainties (1σ) are included.

AGN name	N_0	α	β $\times 10^{-3}$	E_b [MeV]	\hat{B} [nG]	\hat{s} [kpc]
1ES 0033+595	0.629(0.025)	1.54(0.03)	42(12)	3177	911.9(1.5)	911.4(1.3)
3C 66A	12.5(0.2)	1.80(0.01)	43(6)	1211	311.0(44.4)	7.3(1.0)
PKS 0301-243	11.1(0.4)	1.81(0.02)	38(10)	954.4	50660.9(314.0)	1.3(0.01)
NGC 1275	102(2)	1.98(0.01)	85(3)	883.6	14007.6(694.6)	0.2(0.01)
PKS 0447-439	7.09(0.13)	1.56(0.01)	83(6)	1605	2151.5(41.6)	5.5(0.1)
1ES 0502+675	0.083(0.004)	1.38(0.03)	—	6322	830.6(0.7)	1000.0(0.7)
1ES 0806+524	2.31(0.06)	1.79(0.02)	12(10)	1297	74.6(2.4)	435.4(12.4)
1ES 1011+496	7.68(0.10)	1.73(0.01)	17(5)	1066	118.6(0.9)	723.0(5.0)
Markarian 421	19.1(0.2)	1.69(0.005)	13(2)	1286	21.1(4.2)	216.3(18.4)
Markarian 180	0.182(0.008)	1.70(0.03)	—	2679	98.5(1.5)	870.1(11.9)
1ES 1215+303	17.9(0.4)	1.81(0.01)	53(7)	1066	47661.7(202.6)	1.4(0.01)
1ES 1218+304	0.418(0.015)	1.68(0.02)	—	4442	241288.9(42.7)	9.4(0.002)
PKS 1440-389	1.75(0.06)	1.51(0.03)	100(13)	2014	3331.2(38.9)	11.7(0.1)
PG 1553+113	5.66(0.09)	1.45(0.01)	49(5)	1847	3496.4(0.0)	98466.5(0.1)
Markarian 501	8.35(0.34)	1.70(0.01)	17(5)	1478	85669.0(71.4)	3.2(0.003)
1ES 1727+502	0.297(0.017)	1.75(0.03)	—	3005	226832.0(0.6)	690.1(0.002)
1ES 1959+650	3.39(0.06)	1.70(0.01)	9(5)	1733	89.5(0.9)	831.8(10.0)
PKS 2005-489	0.747(0.050)	1.76(0.02)	—	2398	21312.2(78.1)	5.6(0.02)
PKS 2155-304	30.9(0.4)	1.76(0.01)	40(5)	1136	344288.2(57.1)	5.4(0.001)
1ES 2344+514	1.07(0.05)	1.56(0.03)	61(14)	1938	482.4(82.1)	9.2(1.1)

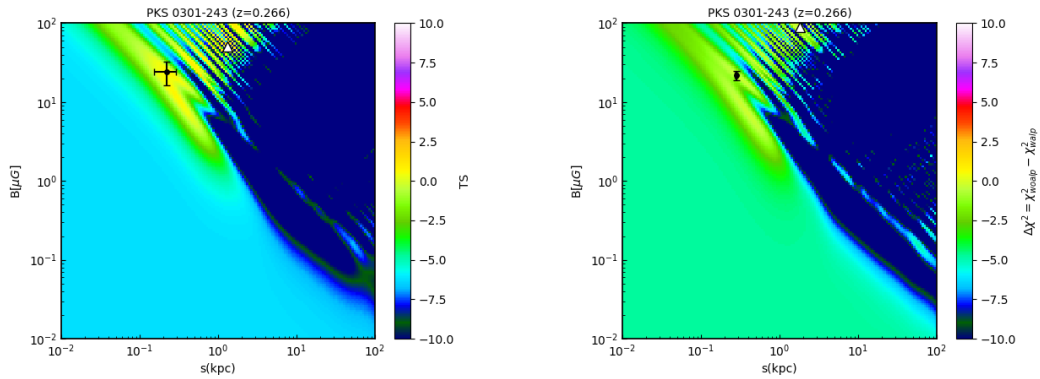


Figure 12. PKS 0301-243, same as Fig. 1.

Table 9. Best-fitting log-likelihood and χ^2 values for null (H_0) and ALP hypotheses (H_1). TS values are calculated with Eqs. (4.6) and (4.7) for likelihood ratio test and $\Delta\chi^2$ test respectively. Corresponding significance levels for both tests are listed as well.

AGN name	H_0 $\ln(L_{max}^0)$	H_1 $\ln(L_{max}^1)$	TS	z -score (H_1/H_0)	H_0 $\chi_{w/oALP}^2/df$	H_1 $\chi_{w/ALP}^2/df$	$\Delta\chi^2$	z -score (H_1/H_0)
1ES 0033+595	712253.0	712257.8	9.6	2.3	22.2/15	13.5/13	8.8	2.0
3C 66A	-122858.4	-122856.5	3.8	2.0	20.6/15	16.3/13	4.3	2.3
PKS 0301-243	-154508.6	-154507.9	1.4	0.6	16.3/15	16.3/13	-0.1	0.5
NGC 1275	26767.7	26777.6	19.8	3.6	25.6/15	22.4/13	3.2	1.8
PKS 0447-439	-146200.2	-146199.1	2.3	2.0	26.2/15	22.6/13	3.6	2.1
1ES 0502+675	-44659.7	-44656.2	7.0	1.3	41.9/16	36.2/14	5.7	1.0
1ES 0806+524	-159751.7	-159750.3	2.9	0.2	20.5/15	16.4/13	4.1	0.5
1ES 1011+496	-153505.0	-153500.7	8.6	1.6	12.7/15	8.0/13	4.7	0.7
Markarian 421								
10yrs LAT	-130615.4	-130606.2	18.5	3.6	28.8/15	15.5/13	13.3	2.7
simul. LAT+MAGIC	—	—	—	—	33.4/15	15.2/13	18.2	1.8
Markarian 180	-132628.4	-132627.7	1.4	0.01	23.8/16	19.8/14	4.0	0.5
1ES 1215+303	-143988.2	-143984.0	8.4	2.2	15.5/15	13.4/13	2.1	1.2
1ES 1218+304	-145577.3	-145576.5	1.6	1.3	19.0/16	19.9/14	-0.9	1.1
PKS 1440-389	60781.3	60783.8	5.0	1.5	18.9/15	16.1/13	2.7	0.8
PG 1553+113	-152448.5	-152447.6	1.7	0.4	17.8/15	14.7/13	3.1	0.5
Markarian 501	-95747.1	-95742.8	8.7	1.7	18.5/15	12.8/13	5.7	1.0
1ES 1727+502	-154208.5	-154205.2	6.8	1.4	26.7/16	22.7/14	3.9	0.3
1ES 1959+650	-49456.2	-49453.1	6.3	1.1	21.6/15	13.5/13	8.1	1.5
PKS 2005-489	-166314.9	-166307.9	13.6	2.5	33.9/16	17.2/14	16.7	2.7
PKS 2155-304								
10yrs LAT	-144503.6	-144502.7	1.7	1.5	15.8/15	14.3/13	1.5	1.1
simul. LAT+H.E.S.S.	—	—	—	—	33.3/18	29.2/16	4.1	1.6
1ES 2344+514	-61482.2	-61480.1	4.3	1.2	15.2/15	13.6/13	1.6	0.6

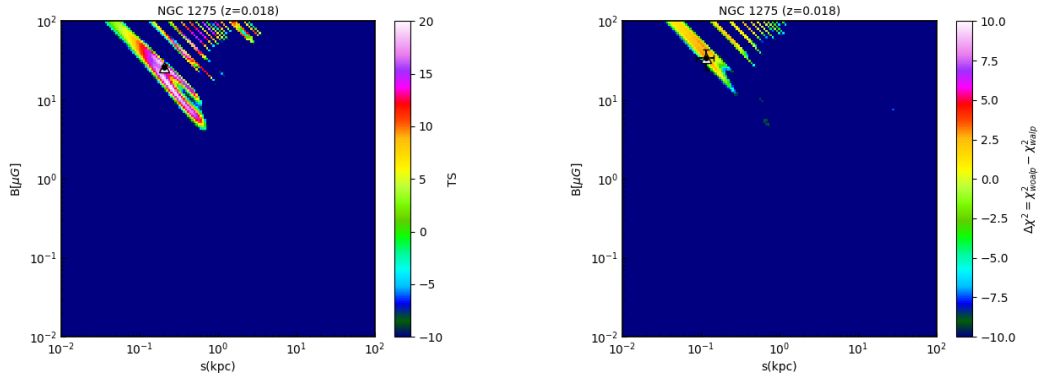


Figure 13. NGC 1275, same as Fig. 1.

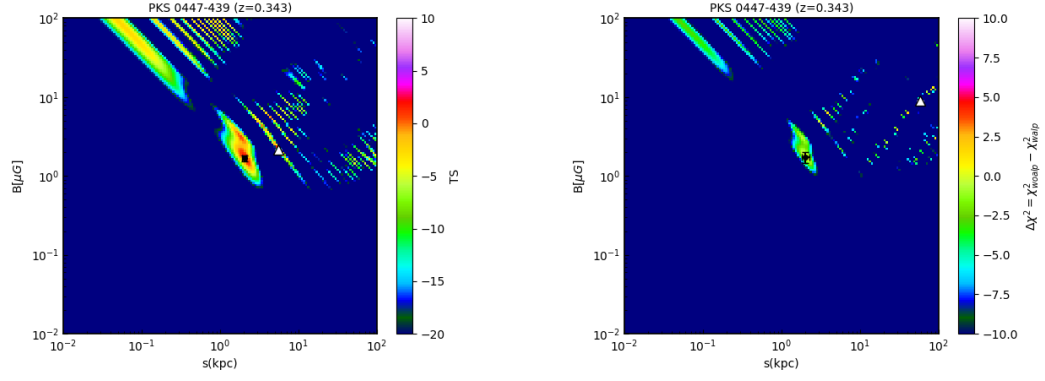


Figure 14. PKS 0447-439, same as Fig. 1.

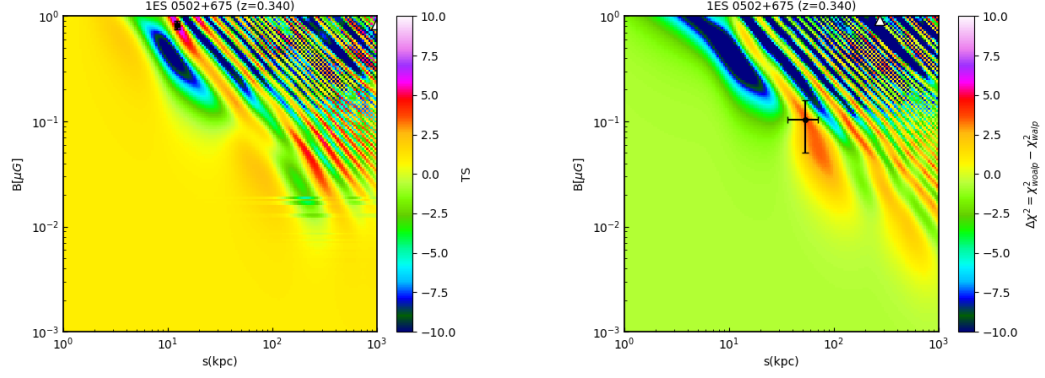


Figure 15. 1E 0502+675, same as Fig. 1.

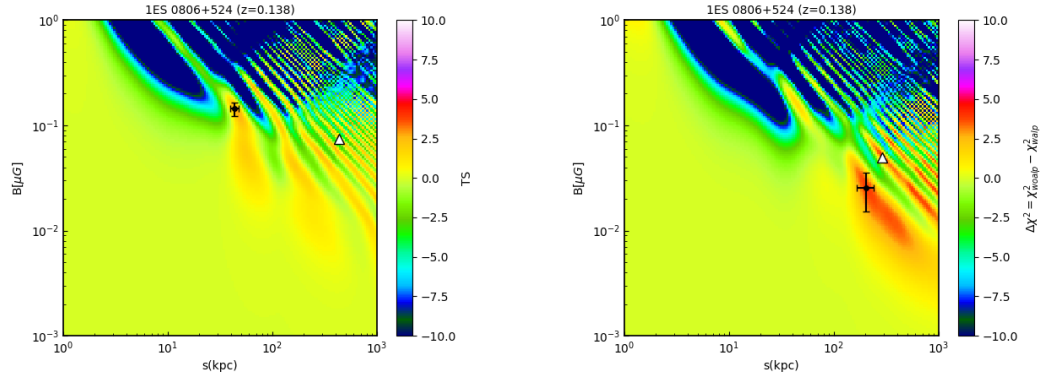


Figure 16. 1ES 0806+524, same as Fig. 1.

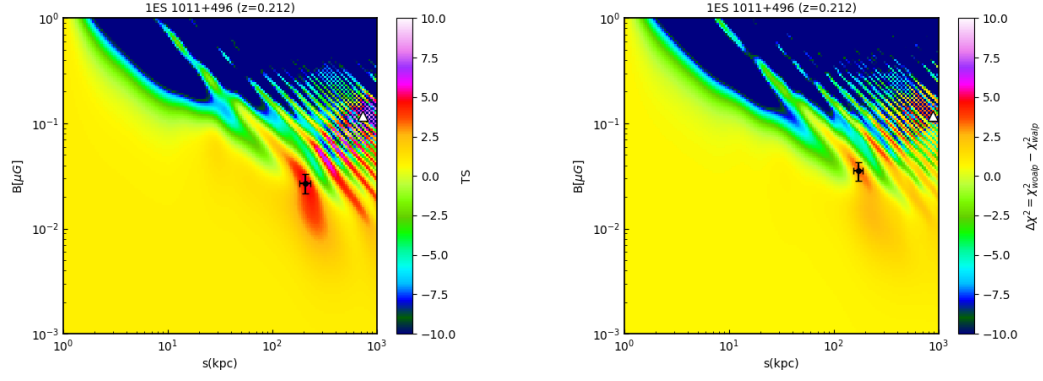


Figure 17. 1ES 1011+496, same as Fig. 1.

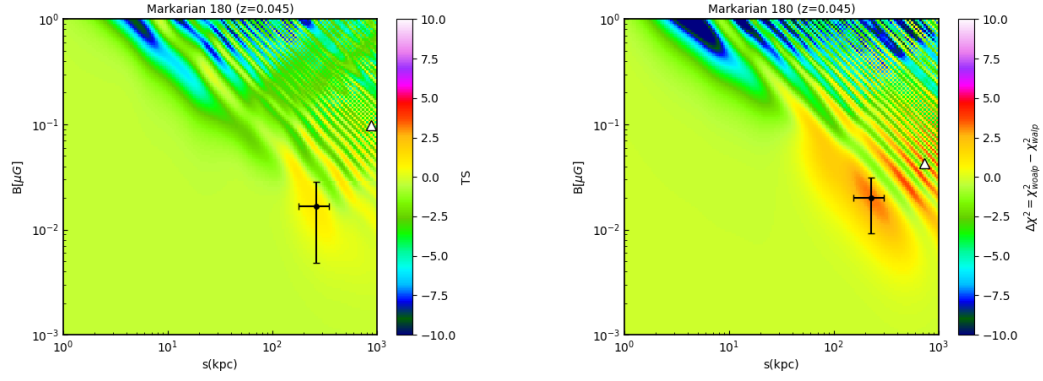


Figure 18. Markarian 180, same as Fig. 1.

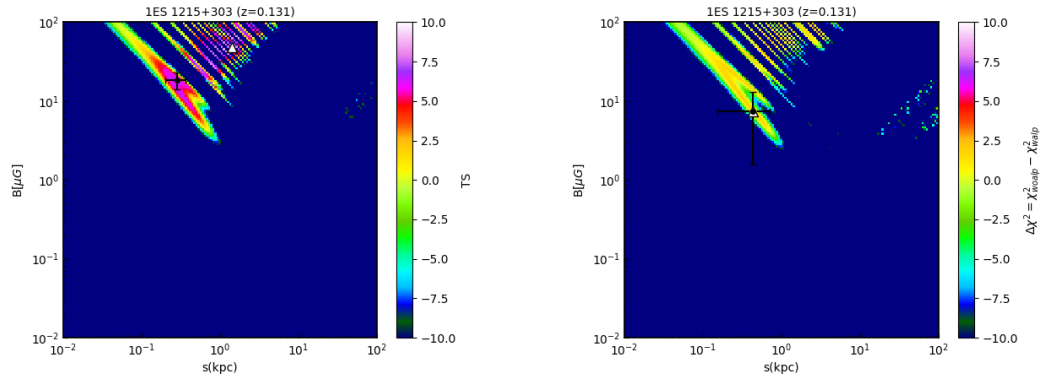


Figure 19. 1ES 1215+303, same as Fig. 1.

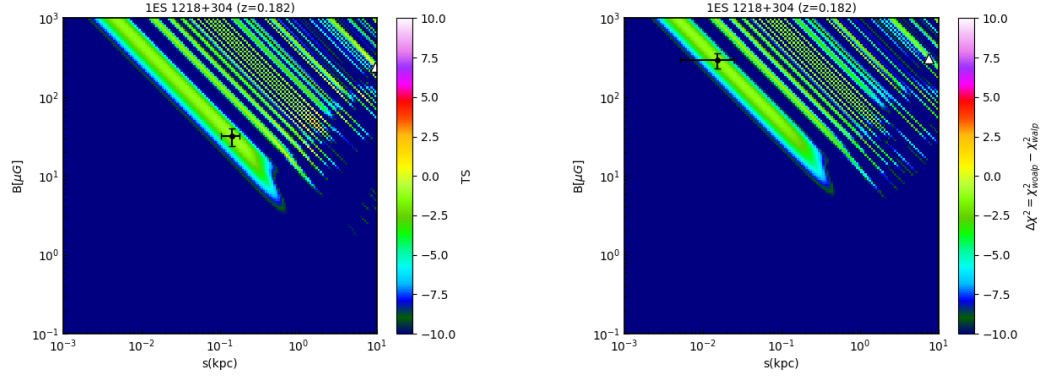


Figure 20. 1ES 1218+304, same as Fig. 1.

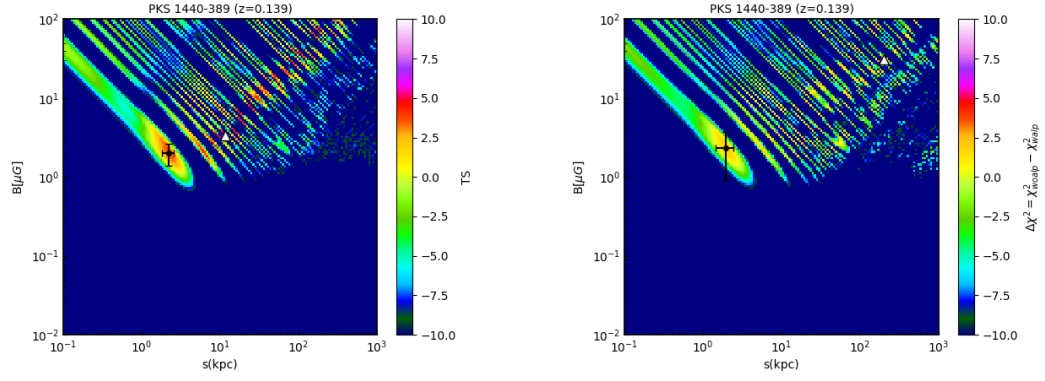


Figure 21. PKS 1440-389, same as Fig. 1.

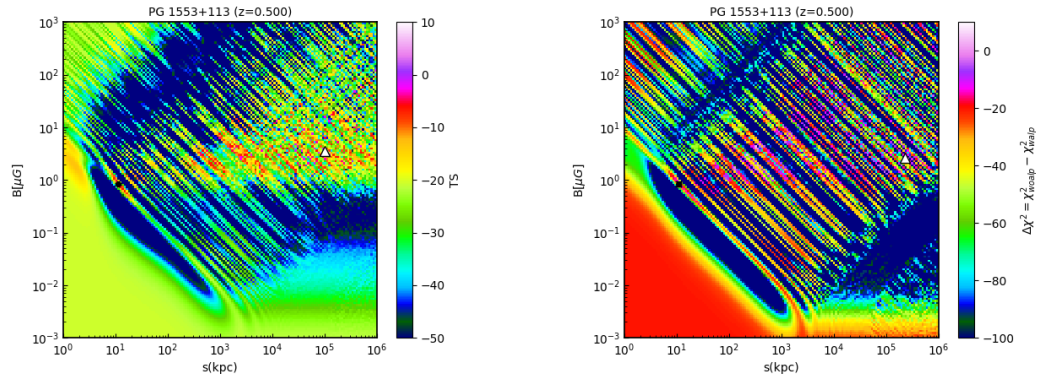


Figure 22. PG 1553+113, same as Fig. 1.

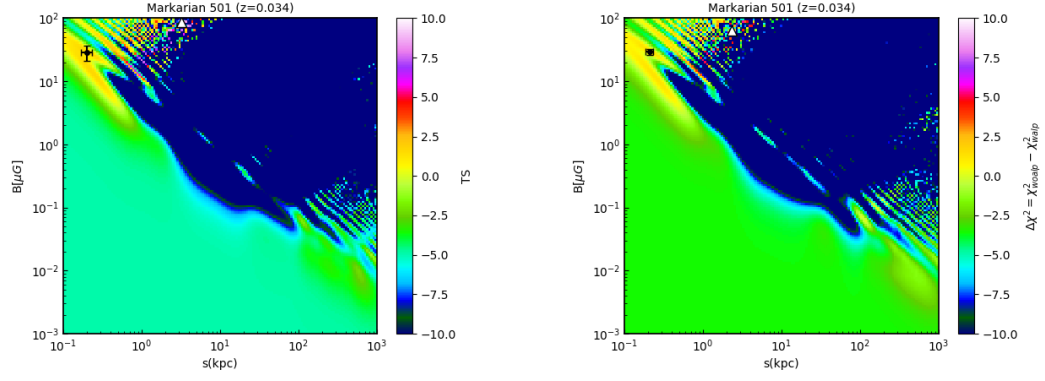


Figure 23. Markarian 501, same as Fig. 1.

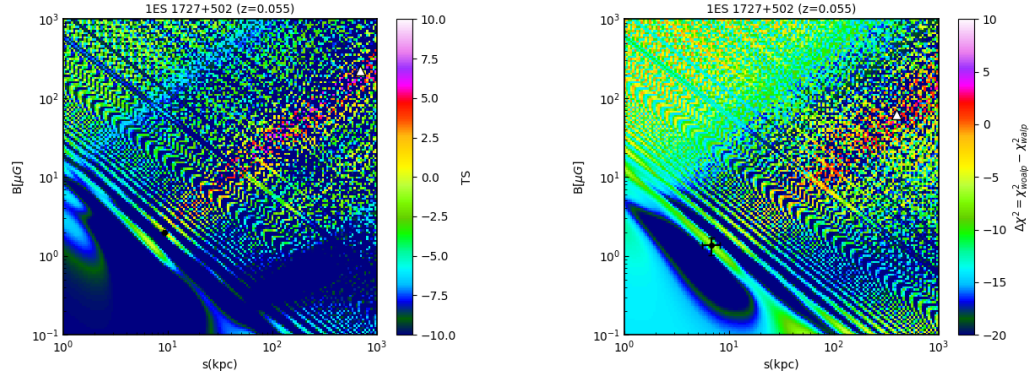


Figure 24. 1ES 1727+502, same as Fig. 1.

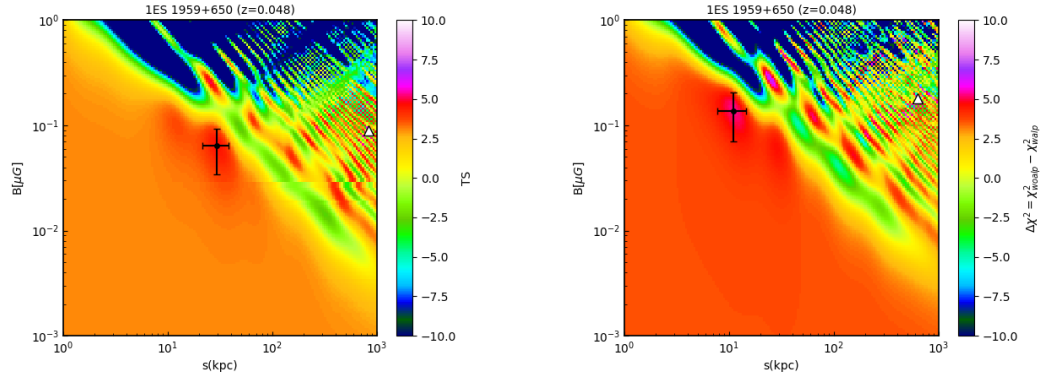


Figure 25. 1ES 1959+650, same as Fig. 1.

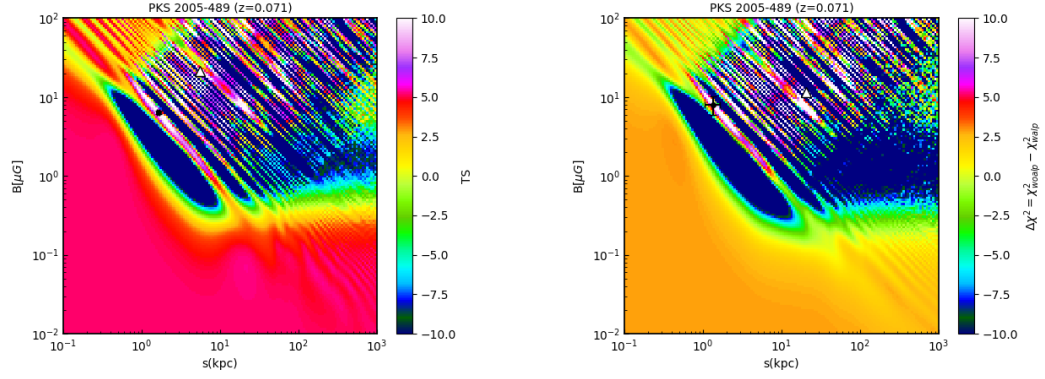


Figure 26. PKS 2005-304, same as Fig. 1.

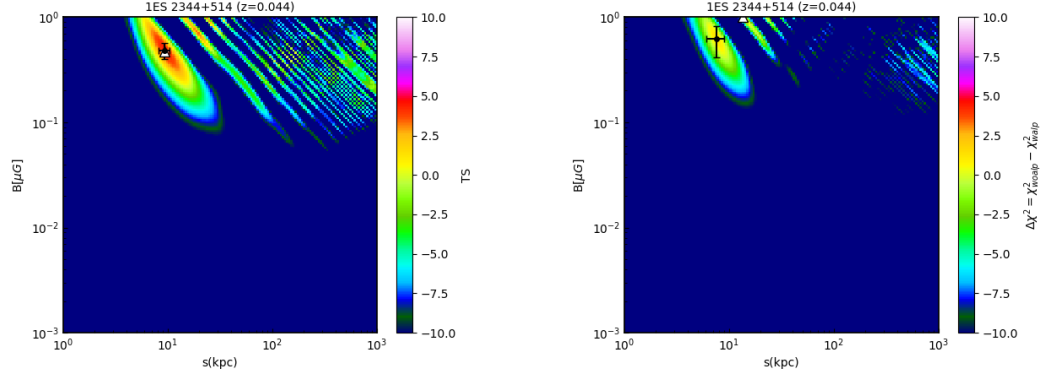


Figure 27. 1ES 2344+514, same as Fig. 1.

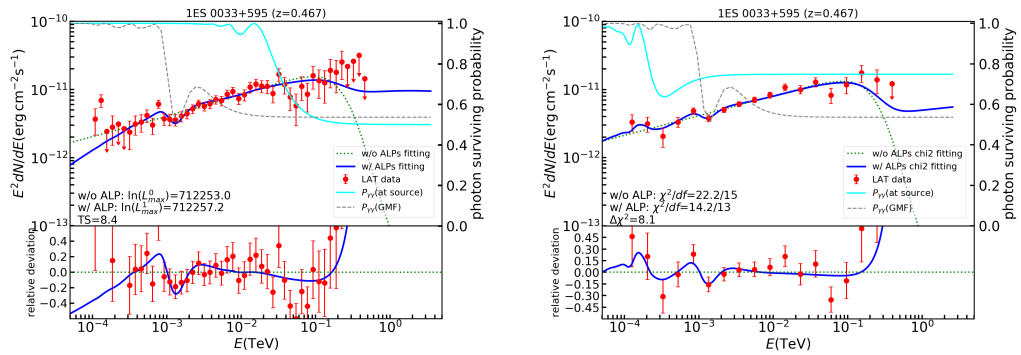


Figure 28. 1ES 0033+595, same as Fig. 2.

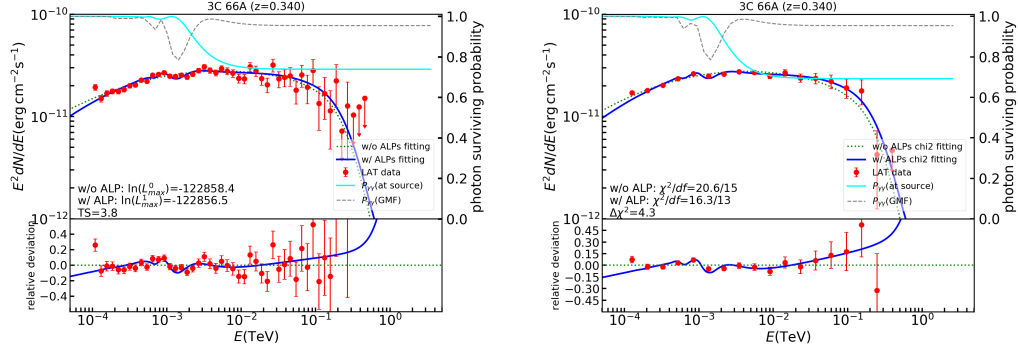


Figure 29. 3C 66A, same as Fig. 2.

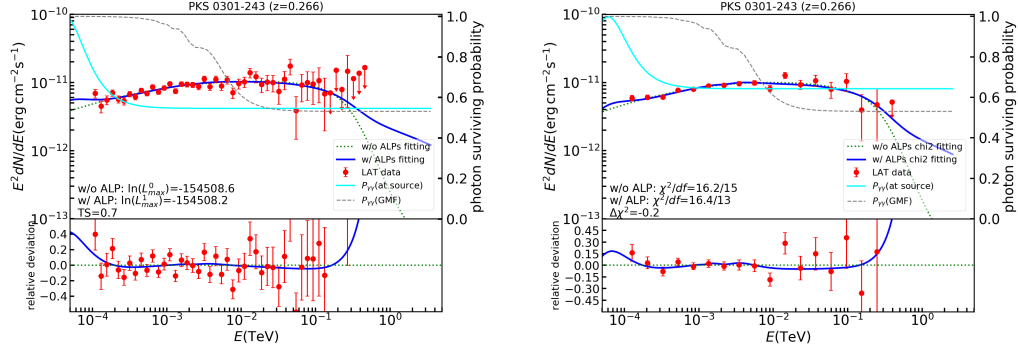


Figure 30. PKS 0301-243, same as Fig. 2.

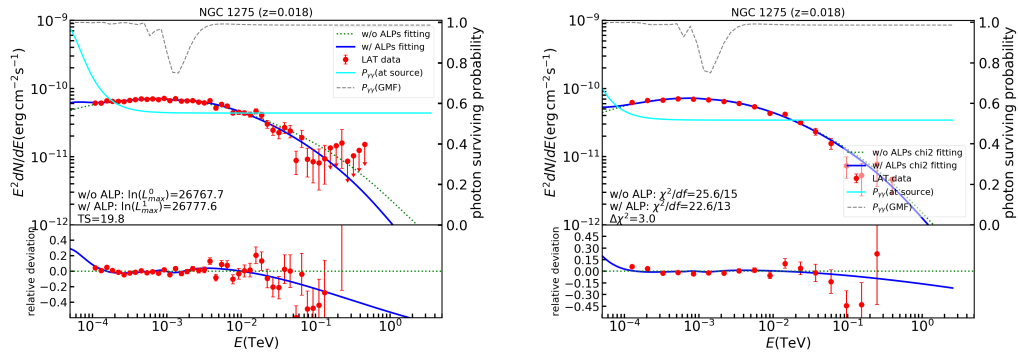


Figure 31. NGC 1275, same as Fig. 2.

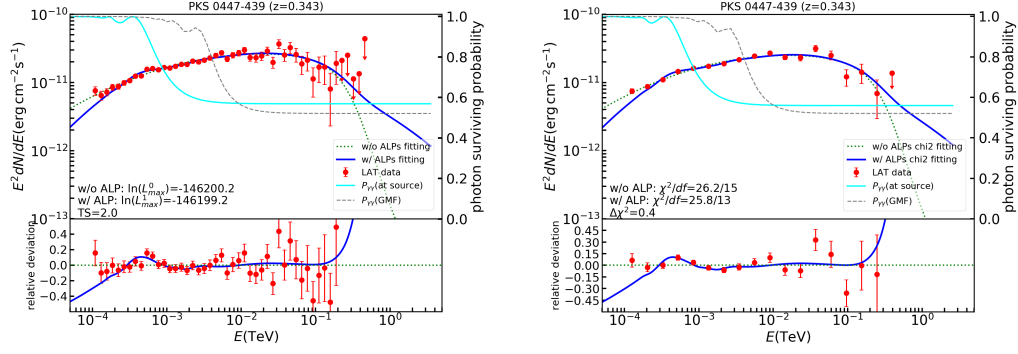


Figure 32. PKS 0447-439, same as Fig. 2.

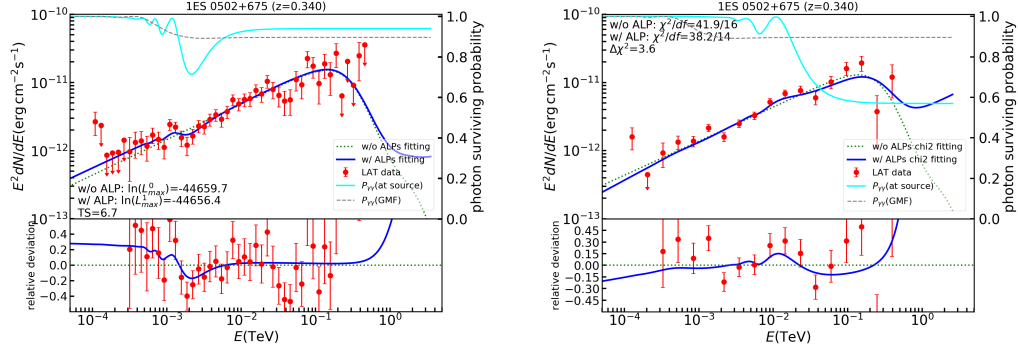


Figure 33. 1ES 0502+675, same as Fig. 2.

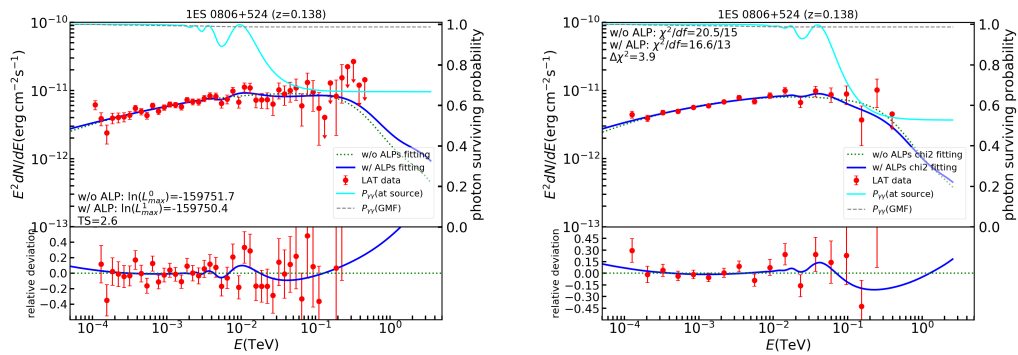


Figure 34. 1ES 0806+524, same as Fig. 2.

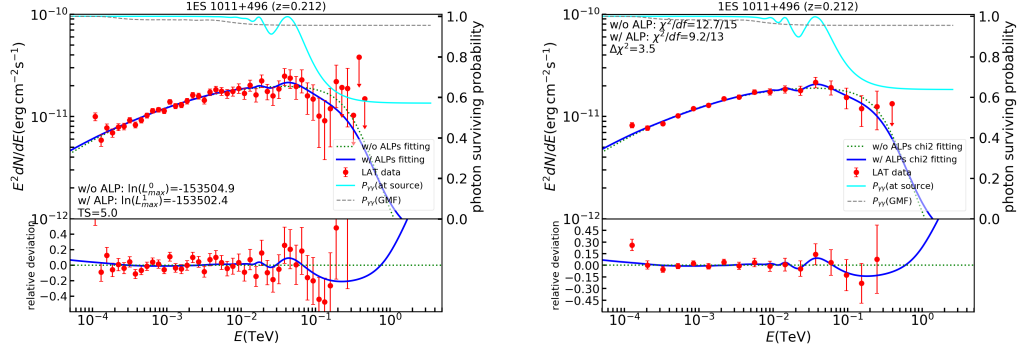


Figure 35. 1ES 1011+496, same as Fig. 2.

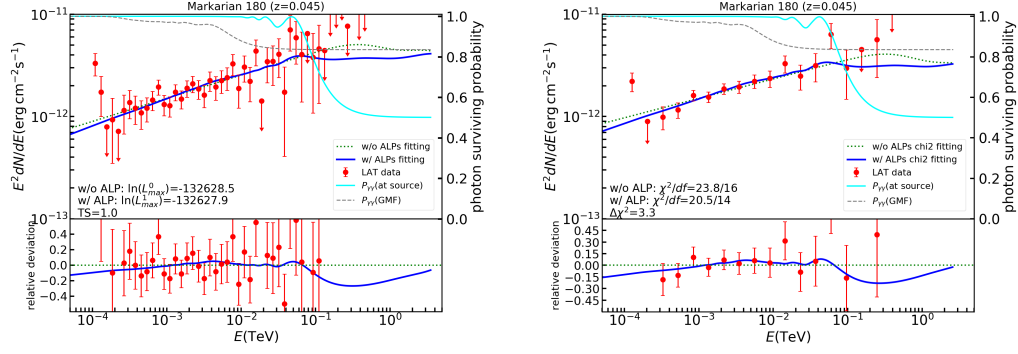


Figure 36. Markarian 180, same as Fig. 2.

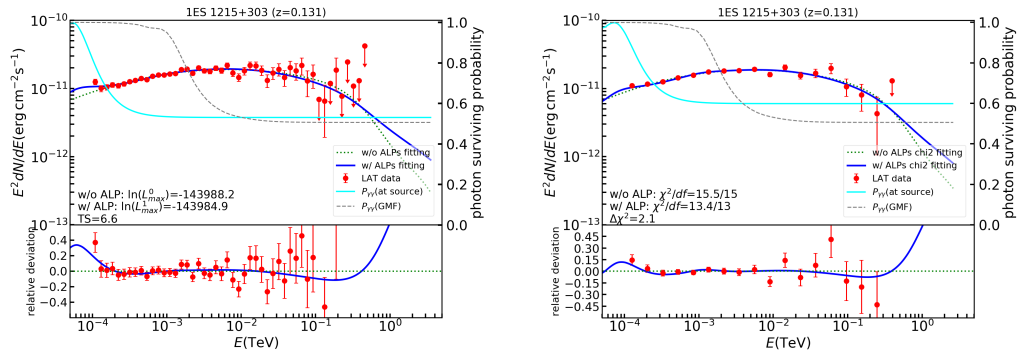


Figure 37. 1ES 1215+303, same as Fig. 2.

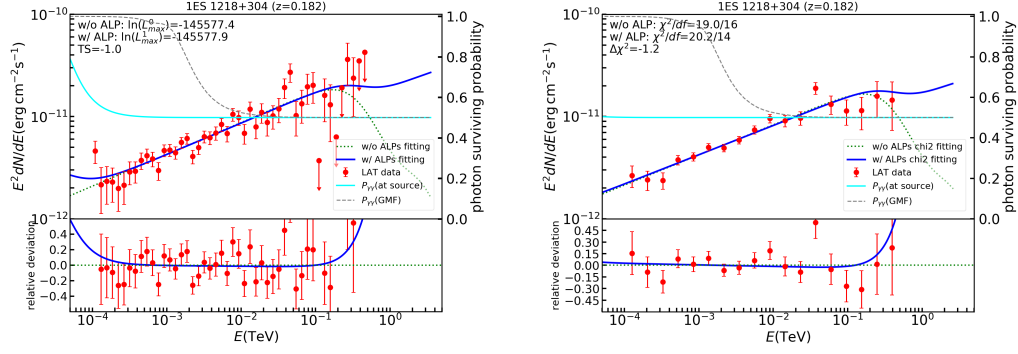


Figure 38. 1ES 1218+304, same as Fig. 2.

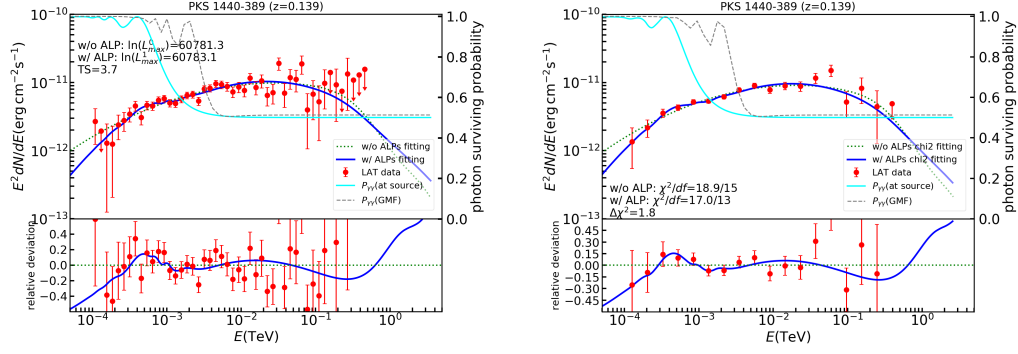


Figure 39. PKS 1440-389, same as Fig. 2.

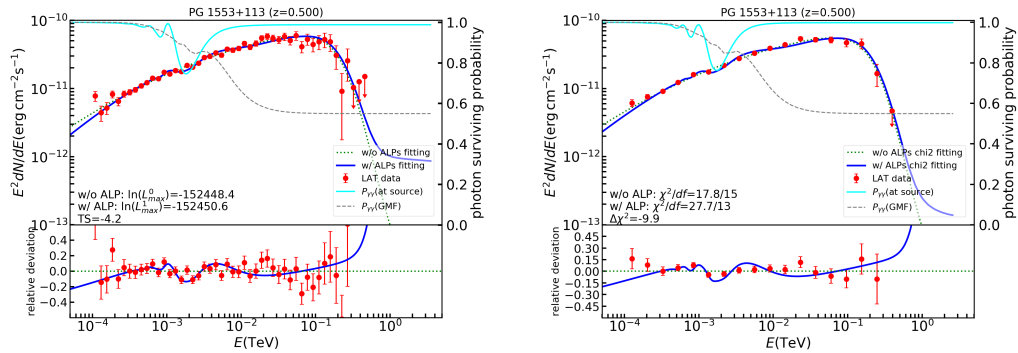


Figure 40. PG 1553+113, same as Fig. 2.

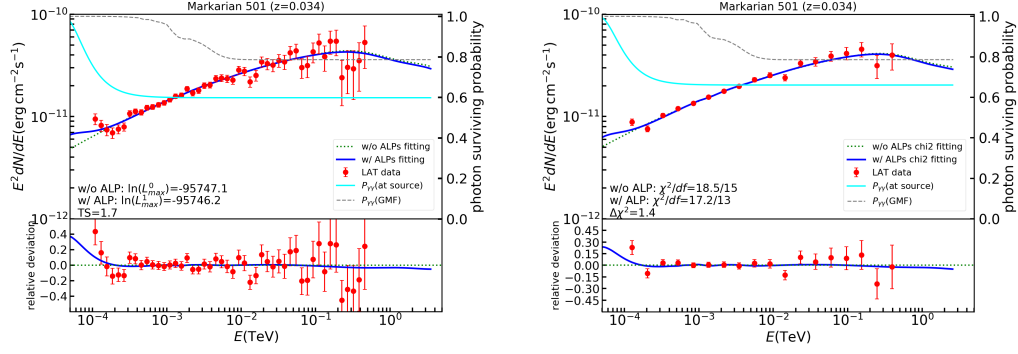


Figure 41. Markarian 501, same as Fig. 2.

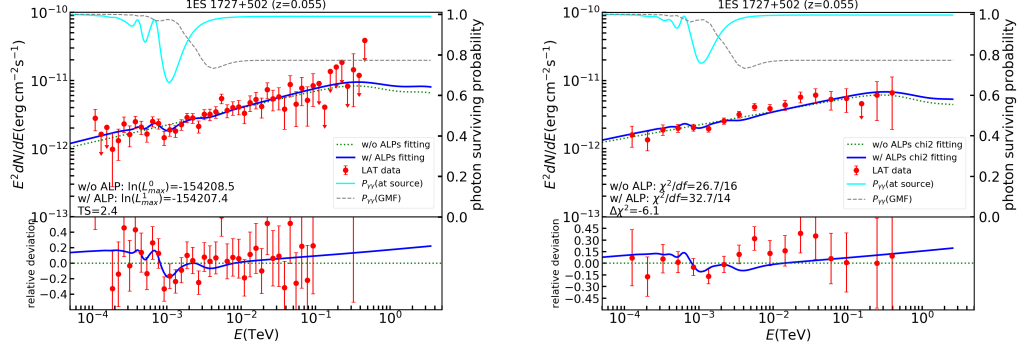


Figure 42. 1ES 1727+502, same as Fig. 2.

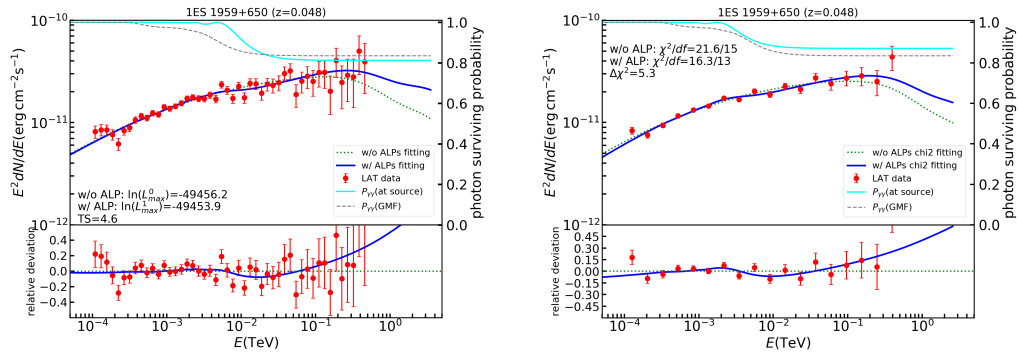


Figure 43. 1ES 1959+650, same as Fig. 2.

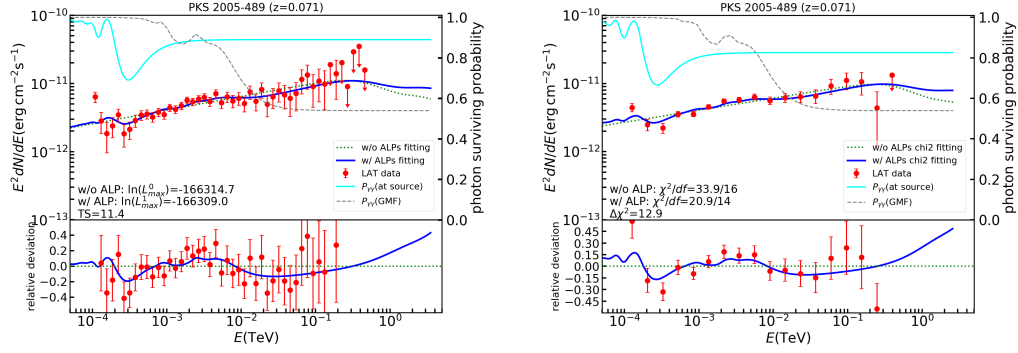


Figure 44. PKS 2005-489, same as Fig. 2.

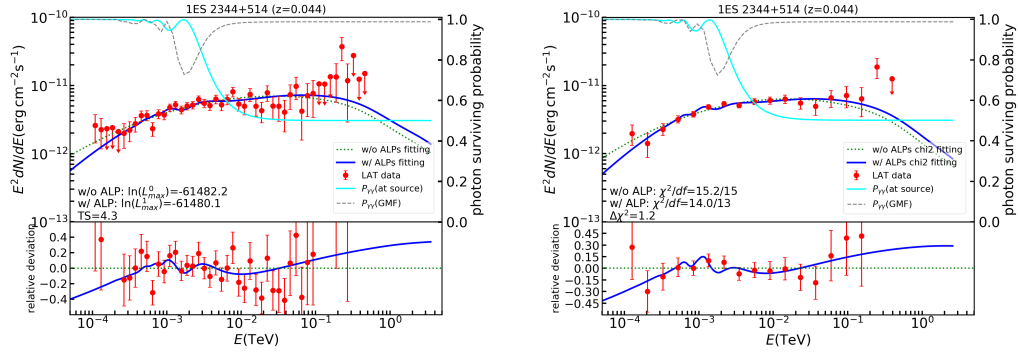


Figure 45. 1ES 2344+514, same as Fig. 2.

References

- [1] R. D. Peccei and Helen R. Quinn. Constraints Imposed by CP Conservation in the Presence of Instantons. *Phys. Rev. D*, 16:1791–1797, 1977.
- [2] R. D. Peccei and Helen R. Quinn. CP Conservation in the Presence of Instantons. *Phys. Rev. Lett.*, 38:1440–1443, 1977.
- [3] Peter Svrcek and Edward Witten. Axions In String Theory. *JHEP*, 06:051, 2006.
- [4] Joseph P. Conlon. The QCD axion and moduli stabilisation. *JHEP*, 05:078, 2006.
- [5] Michele Cicoli, Mark Goodsell, and Andreas Ringwald. The type IIB string axiverse and its low-energy phenomenology. *JHEP*, 10:146, 2012.
- [6] John Preskill, Mark B. Wise, and Frank Wilczek. Cosmology of the Invisible Axion. *Phys. Lett. B*, 120:127–132, 1983.
- [7] L. F. Abbott and P. Sikivie. A Cosmological Bound on the Invisible Axion. *Phys. Lett. B*, 120:133–136, 1983.
- [8] Michael Dine and Willy Fischler. The Not So Harmless Axion. *Phys. Lett. B*, 120:137–141, 1983.
- [9] Joerg Jaeckel. A Family of WISPy Dark Matter Candidates. *Phys. Lett. B*, 732:1–7, 2014.
- [10] Alessandro De Angelis, Oriana Mansutti, and Marco Roncadelli. Axion-Like Particles, Cosmic Magnetic Fields and Gamma-Ray Astrophysics. *Phys. Lett. B*, 659:847–855, 2008.
- [11] Dan Hooper and Pasquale D. Serpico. Detecting Axion-Like Particles With Gamma Ray Telescopes. *Phys. Rev. Lett.*, 99:231102, 2007.
- [12] Melanie Simet, Dan Hooper, and Pasquale D. Serpico. The Milky Way as a Kiloparsec-Scale Axionscope. *Phys. Rev. D*, 77:063001, 2008.
- [13] Alessandro De Angelis, Giorgio Galanti, and Marco Roncadelli. Relevance of axion-like particles for very-high-energy astrophysics. *Phys. Rev. D*, 84:105030, 2011. [Erratum: *Phys.Rev.D* 87, 109903 (2013)].
- [14] Dieter Horns, Luca Maccione, Manuel Meyer, Alessandro Mirizzi, Daniele Montanino, and Marco Roncadelli. Hardening of TeV gamma spectrum of AGNs in galaxy clusters by conversions of photons into axion-like particles. *Phys. Rev. D*, 86:075024, 2012.
- [15] G. I. Rubtsov and S. V. Troitsky. Breaks in gamma-ray spectra of distant blazars and transparency of the Universe. *JETP Lett.*, 100(6):355–359, 2014.
- [16] Maxim Libanov and Sergey Troitsky. On the impact of magnetic-field models in galaxy clusters on constraints on axion-like particles from the lack of irregularities in high-energy spectra of astrophysical sources. *Phys. Lett. B*, 802:135252, 2020.
- [17] Jhilik Majumdar, Francesca Calore, and Dieter Horns. Search for gamma-ray spectral modulations in Galactic pulsars. *JCAP*, 04:048, 2018.
- [18] Manuel Meyer, Dieter Horns, and Martin Raue. First lower limits on the photon-axion-like particle coupling from very high energy gamma-ray observations. *Phys. Rev. D*, 87(3):035027, 2013.
- [19] Kazunori Kohri and Hideo Kodama. Axion-Like Particles and Recent Observations of the Cosmic Infrared Background Radiation. *Phys. Rev. D*, 96(5):051701, 2017.
- [20] Robin Bähre et al. Any light particle search II —Technical Design Report. *JINST*, 8:T09001, 2013.
- [21] V. Anastassopoulos et al. New CAST Limit on the Axion-Photon Interaction. *Nature Phys.*, 13:584–590, 2017.

- [22] Gautham Adamane Pallathadka et al. Reconciling hints on axion-like-particles from high-energy gamma rays with stellar bounds. *JCAP*, 11:036, 2021.
- [23] Georg Raffelt and Leo Stodolsky. Mixing of the Photon with Low Mass Particles. *Phys. Rev. D*, 37:1237, 1988.
- [24] Alessandro Mirizzi, Georg G. Raffelt, and Pasquale D. Serpico. Photon-axion conversion as a mechanism for supernova dimming: Limits from CMB spectral distortion. *Phys. Rev. D*, 72:023501, 2005.
- [25] Alessandro Mirizzi, Georg G. Raffelt, and Pasquale D. Serpico. Photon-axion conversion in intergalactic magnetic fields and cosmological consequences. *Lect. Notes Phys.*, 741:115–134, 2008.
- [26] Giorgio Galanti, Fabrizio Tavecchio, Marco Roncadelli, and Carmelo Evoli. Blazar VHE spectral alterations induced by photon–ALP oscillations. *Mon. Not. Roy. Astron. Soc.*, 487(1):123–132, 2019.
- [27] Alexandra Dobrynina, Alexander Kartavtsev, and Georg Raffelt. Photon-photon dispersion of TeV gamma rays and its role for photon-ALP conversion. *Phys. Rev. D*, 91:083003, 2015. [Erratum: *Phys.Rev.D* 95, 109905 (2017)].
- [28] Csaba Csaki, Nemanja Kaloper, Marco Peloso, and John Terning. Super GZK photons from photon axion mixing. *JCAP*, 05:005, 2003.
- [29] M. S. Pshirkov, P. G. Tinyakov, and F. R. Urban. New limits on extragalactic magnetic fields from rotation measures. *Phys. Rev. Lett.*, 116(19):191302, 2016.
- [30] Ruth Durrer and Andrii Neronov. Cosmological Magnetic Fields: Their Generation, Evolution and Observation. *Astron. Astrophys. Rev.*, 21:62, 2013.
- [31] Ronnie Jansson and Glennys R. Farrar. A New Model of the Galactic Magnetic Field. *Astrophys. J.*, 757:14, 2012.
- [32] M. Ajello et al. The Fourth Catalog of Active Galactic Nuclei Detected by the Fermi Large Area Telescope. *Astrophys. J.*, 892:105, 2020.
- [33] Jeremy S. Sanders, A. C. Fabian, and R. J. H. Dunn. Non-thermal x-rays, a high abundance ridge and fossil bubbles in the core of the Perseus cluster of galaxies. *Mon. Not. Roy. Astron. Soc.*, 360:133–140, 2005.
- [34] G. B. Taylor, N. E. Gugliucci, A. C. Fabian, J. S. Sanders, Gianfranco Gentile, and S. W. Allen. Magnetic fields in the center of the perseus cluster. *Mon. Not. Roy. Astron. Soc.*, 368:1500–1506, 2006.
- [35] M. Ajello et al. Search for Spectral Irregularities due to Photon–Axionlike-Particle Oscillations with the Fermi Large Area Telescope. *Phys. Rev. Lett.*, 116(16):161101, 2016.
- [36] Matthew Wood, Regina Caputo, Eric Charles, Mattia Di Mauro, Jeffrey Magill, and Jeremy Perkins. Fermipy: An open-source Python package for analysis of Fermi-LAT Data. *PoS, ICRC2017:824*, 2018.
- [37] S. Abdollahi et al. *Fermi* Large Area Telescope Fourth Source Catalog. *Astrophys. J. Suppl.*, 247(1):33, 2020.
- [38] A. Dominguez et al. Extragalactic Background Light Inferred from AEGIS Galaxy SED-type Fractions. *Mon. Not. Roy. Astron. Soc.*, 410:2556, 2011.
- [39] S. S. Wilks. The Large-Sample Distribution of the Likelihood Ratio for Testing Composite Hypotheses. *Annals Math. Statist.*, 9(1):60–62, 1938.
- [40] P. M. Chadwick, K. Lyons, T. J. L. McComb, S. McQueen, K. J. Orford, J. L. Osborne, S. M. Rayner, S. E. Shaw, K. E. Turver, and G. J. Wieczorek. Pks 2155-304 - a source of vhe gamma-rays. *Astropart. Phys.*, 11(1-2):145–148, 1999.

- [41] A. Abramowski et al. VHE gamma-ray emission of PKS 2155-304: spectral and temporal variability. *Astron. Astrophys.*, 520:A83, 2010.
- [42] H. Abdalla et al. Gamma-ray blazar spectra with H.E.S.S. II mono analysis: The case of PKS 2155–304 and PG 1553+113. *Astron. Astrophys.*, 600:A89, 2017.
- [43] M. Punch et al. Detection of TeV photons from the active galaxy Markarian 421. *Nature*, 358:477–478, 1992.
- [44] A. A. Abdo et al. Fermi large area telescope observations of Markarian 421: The missing piece of its spectral energy distribution. *Astrophys. J.*, 736:131, 2011.
- [45] Manuel Meyer and J. Conrad. Sensitivity of the Cherenkov Telescope Array to the detection of axion-like particles at high gamma-ray opacities. *JCAP*, 12:016, 2014.
- [46] Fabrizio Tavecchio, Marco Roncadelli, and Giorgio Galanti. Photons to axion-like particles conversion in Active Galactic Nuclei. *Phys. Lett. B*, 744:375–379, 2015.
- [47] Ilana Feain, Ronald Ekers, Tara Murphy, Bryan Gaensler, J-P Macquart, Raymond Norris, Tim Cornwell, Melanie Johnston-Hollitt, Juergen Ott, and Enno Middelberg. Faraday Rotation Structure on Kiloparsec Scales in the Giant Radio Lobes of Centaurus A. *Astrophys. J.*, 707:114–125, 2009.
- [48] K. T. Kim, P. P. Kronberg, P. E. Dewdney, and T. L. Landecker. The Halo and Magnetic Field of the Coma Cluster of Galaxies. *Astrophys. J.*, 355:29, May 1990.
- [49] C. L. Carilli and G. B. Taylor. Cluster magnetic fields. *Ann. Rev. Astron. Astrophys.*, 40:319–348, 2002.
- [50] Federica Govoni and Luigina Feretti. Magnetic field in clusters of galaxies. *Int. J. Mod. Phys. D*, 13:1549–1594, 2004.
- [51] Kandaswamy Subramanian, Anvar Shukurov, and Nils Erland L. Haugen. Evolving turbulence and magnetic fields in galaxy clusters. *Mon. Not. Roy. Astron. Soc.*, 366:1437–1454, 2006.
- [52] Takuya Akahori and Dongsu Ryu. Faraday Rotation Measure due to the Intergalactic Magnetic Field. *Astrophys. J.*, 723:476–481, 2010.
- [53] V. Heesen, S. P. O’Sullivan, M. Brüggen, A. Basu, R. Beck, A. Seta, E. Carretti, M. G. H. Krause, M. Haverkorn, S. Hutschenreuter, A. Bracco, M. Stein, D. J. Bomans, R. J. Dettmar, K. T. Chyży, G. H. Heald, R. Paladino, and C. Horellou. Detection of magnetic fields in the circumgalactic medium of nearby galaxies using Faraday rotation. *Astron. Astrophys.*, 670:L23, February 2023.
- [54] Tessa Vernstrom, Bryan M. Gaensler, Shea Brown, Emil Lenc, and Ray P. Norris. Low Frequency Radio Constraints on the Synchrotron Cosmic Web. *Mon. Not. Roy. Astron. Soc.*, 467(4):4914–4936, 2017.
- [55] S. Brown, T. Vernstrom, E. Carretti, K. Dolag, B. M. Gaensler, L. Staveley-Smith, G. Bernardi, M. Haverkorn, M. Kesteven, and S. Poppi. Limiting Magnetic Fields in the Cosmic Web with Diffuse Radio Emission. *Mon. Not. Roy. Astron. Soc.*, 468(4):4246–4253, 2017.
- [56] Valentina Vacca et al. Observations of a nearby filament of galaxy clusters with the Sardinia Radio Telescope. *Mon. Not. Roy. Astron. Soc.*, 479(1):776–806, 2018.
- [57] S. P. O’Sullivan et al. The intergalactic magnetic field probed by a giant radio galaxy. *Astron. Astrophys.*, 622:A16, 2019.
- [58] Nicola Locatelli, Franco Vazza, Annalisa Bonafede, Serena Banfi, Gianni Bernardi, Claudio Gheller, Andrea Botteon, and Timothy Shimwell. New constraints on the magnetic field in cosmic web filaments. *Astron. Astrophys.*, 652:A80, 2021.
- [59] Tessa Vernstrom, George Heald, Franco Vazza, T. J. Galvin, Jennifer West, Nicola Locatelli, Nicolao Fornengo, and Elena Pinetti. Discovery of magnetic fields along stacked cosmic

- filaments as revealed by radio and X-ray emission. *Mon. Not. Roy. Astron. Soc.*, 505(3):4178–4196, 2021.
- [60] Ettore Carretti et al. Magnetic field strength in cosmic web filaments. *Mon. Not. Roy. Astron. Soc.*, 512(1):945–959, 2022.
 - [61] F. Yusef-Zadeh, J. W. Hewitt, M. Wardle, V. Tatischeff, D. A. Roberts, W. Cotton, H. Uchiyama, M. Nobukawa, T. G. Tsuru, C. Heinke, and M. Royster. Interacting Cosmic Rays with Molecular Clouds: A Bremsstrahlung Origin of Diffuse High-energy Emission from the Inner $2^\circ \times 1^\circ$ of the Galactic Center. *Astrophys. J.*, 762(1):33, January 2013.
 - [62] Federico Marinacci et al. First results from the IllustrisTNG simulations: radio haloes and magnetic fields. *Mon. Not. Roy. Astron. Soc.*, 480(4):5113–5139, 2018.
 - [63] Volker Springel et al. First results from the IllustrisTNG simulations: matter and galaxy clustering. *Mon. Not. Roy. Astron. Soc.*, 475(1):676–698, 2018.
 - [64] A. P. Gautham, Francesca Calore, Pierluca Carenza, Maurizio Giannotti, Dieter Horns, Julian Kuhlmann, Jhilik Majumdar, Alessandro Mirizzi, Andreas Ringwald, Anton Sokolov, Franziska Stief, and Qixin Yu. Reconciling hints on axion-like-particles from high-energy gamma rays with stellar bounds. *JCAP*, 2021(11):036, November 2021.
 - [65] Christopher Dessert, David Dunskey, and Benjamin R. Safdi. Upper limit on the axion-photon coupling from magnetic white dwarf polarization. *Phys. Rev. D*, 105(10):103034, May 2022.